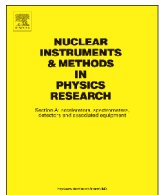




Contents lists available at ScienceDirect

# Nuclear Instruments and Methods in Physics Research A

journal homepage: [www.elsevier.com/locate/nima](http://www.elsevier.com/locate/nima)

## The gas electron multiplier (GEM): Operating principles and applications

Fabio Sauli

CERN, Geneva, Switzerland



### ARTICLE INFO

Available online 7 August 2015

## Keywords:

Gas Electron Multiplier

GEM

Gaseous radiation detectors

### ABSTRACT

Introduced by the author in 1997, The Gas Electron Multiplier (GEM) constitutes a powerful addition to the family of fast radiation detectors; originally developed for particle physics experiments, the device has spawned a large number of developments and applications; a web search yields more than 400 articles on the subject. This note is an attempt to summarize the status of the design, developments and applications of the new detector.

© 2015 CERN for the benefit of the Authors. Published by Elsevier B.V. This is an open access article under the CC BY license (<http://creativecommons.org/licenses/by/4.0/>).

### 1. Introduction

Modern high energy physics experimentation has seen a continuing pursuit between increasingly powerful particle accelerators and more performing detectors. A major revolution occurred in 1968, when CERN's Georges Charpak invented the Multiwire Proportional Chamber (MWPC), a gaseous detector outperforming by orders of magnitude the rate capability of contemporary devices [1]. Consisting of a grid of thin, parallel anode wires between two cathode planes, on application of suitable voltages the device collects and amplifies, by avalanche multiplication, the tiny ionization clusters released in a gas by ionizing radiation, permitting detection with electronics means.

The MWPC was quickly adopted and successfully used by many experiments. Owing to the development work in many groups, the basic structure evolved and diversified into several more sophisticated devices exploiting the measurement of the collection or drift time of electrons to the anodes, or the recording of the signals induced on cathodes to improve time and space resolutions. For an historical survey of these developments, and a description of the detectors operating performances see for example the author's recently published textbook [2].

Despite their successful use in particle physics experiments and other fields, MWPCs have several limitations, intrinsic in their conception. The creation in the multiplication process of large amounts of positive ions, slowly receding towards the cathodes, causes a modification of the applied electric field, and results in a drop of gain and efficiency at particle fluxes above  $\sim 10^4 \text{ mm}^{-2}$  [3]. The discrete wire spacing is itself a limitation to the multi-track resolution, essential at high particle rates and multiplicities. Even more detrimental, the creation and deposit on the anode wires of

thin insulating layers caused by the polymerization of organic gases or pollutants may result in an amazingly short operating life span [4].

The Micro-Strip Gas Counter (MSGC), introduced by Anton Oed in 1988, seemed to overcome some of the abovementioned limitations [5]. Consisting of a set of thin parallel metallic strips laid on an insulating substrate, alternatively connected as anodes and cathodes, MSGCs provide rate capabilities two orders of magnitude higher than MWPCs, and a tenfold improvement in the multi-track resolution [6]. Disappointingly, and despite the efforts by many groups, the device appeared to be rather susceptible to irreversible degradation due to occasional but destructive discharges.

The problems met with the MSGCs resulted in a large effort devoted to the development of sturdier structures, preserving its rate and multi-track capabilities (for a review, see [7]). Collectively named Micro-Pattern Gas Detectors (MPGD), the new structures are already used in many experimental setups, and are currently the subject of extensive research [8,9]. The present note describes the development and applications of one of these innovative devices, the Gas Electron Multiplier (GEM), invented by the author in 1997 [10,11].

### 2. The gas electron multiplier

Many of the problems encountered with MSGCs are connected to the use of fragile electrodes exposed to the high electric fields needed to achieve the gains, typically around  $10^4$ , needed for detection of small ionization yields. Under these conditions, the occurrence in the gas of rare but highly ionizing events, due for example to neutron or gamma conversions, may lead to the creation of a local charge density exceeding the so-called Raether limit ( $\sim 10^7$  electron-ion pairs) leading to the formation of a streamer, and eventually to a discharge.

A similar problem was met by the author decades ago in the attempt to detect single electrons using a MWPC filled with

E-mail address: [fabio.sauli@cern.ch](mailto:fabio.sauli@cern.ch)

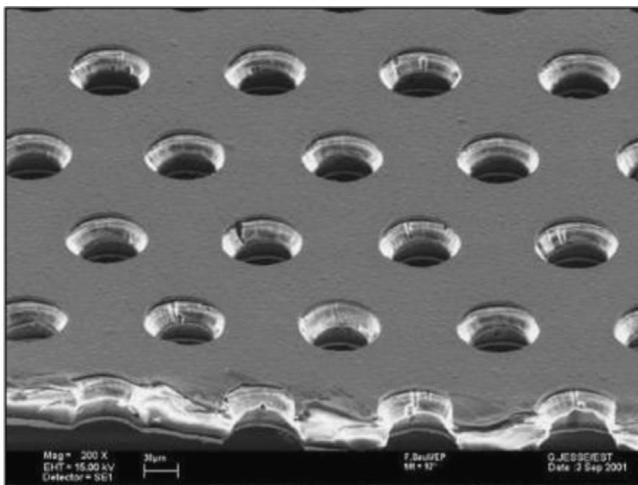


**Fig. 1.** Electron microscope picture of a section of typical GEM electrode, 50  $\mu\text{m}$  thick. The holes pitch and diameter are 140 and 70  $\mu\text{m}$ , respectively.

photosensitive gases. A novel device, the Multi-step Avalanche Chamber, overcame the difficulty introducing the concept of pre-amplification: a region of high field between two meshes used to impart to the primary ionization electrons a first boost of gain, before transferring the charge to a second amplifying structure [12]. The combined amplification of the cascaded assembly, each operated below the critical gain for discharges, added to the suppression of photon-mediated feedback processes due to self-absorption in the gas achieve the successful detection and localization of single photoelectrons for Cherenkov Ring Imaging applications [13].

Inspired by the same basic concept, the Gas Electron Multiplier electrode is a thin polymer foil, metal-coated on both sides and pierced with a high density of holes, typically 50–100  $\text{mm}^{-2}$  (Fig. 1). Inserted between a drift and a charge collection electrode, and with the application of appropriate potentials, the GEM electrode develops near the holes field lines and equipotential as shown in Fig. 2. The large difference of potential applied between the two sides of the foil creates a high field in the holes; electrons released in the upper region drift towards the holes and acquire sufficient energy to cause ionizing collisions with the molecules of the gas filling the structure. A sizeable fraction of the electrons produced in the avalanche's front leave the multiplication region and transfer into the lower section of the structure, where they can be collected by an electrode, or injected into a second multiplying region. Fig. 3 shows schematically a single GEM detector, with a two-dimensional patterned charge detection anode. Unlike other gaseous counters, the (negative) signal on the anode is generated only by the collection of electrons, without a contribution from the slow positive ions, making the device potentially very fast and minimizing space charge problems. Moreover, the low field gap between multiplying and sensing electrodes reduces the probability of the propagation of a discharge to the fragile front-end readout electronics. The equal and opposite charges sensed on the bottom GEM electrode can be used as energy trigger, permitting the detection and localization of events caused by neutral radiation.

Replicated in a cascade of GEM foils, the pre-amplification and transfer process permit one to attain very high proportional gains without the occurrence of discharges, as will be discussed in the next sections.

### 3. Optimization of the GEM geometry and operating conditions

The holes' diameter and shape have a direct influence on the performance and long-term stability of operation of a detector; for a detailed discussion on this point see Section 6. It was found already

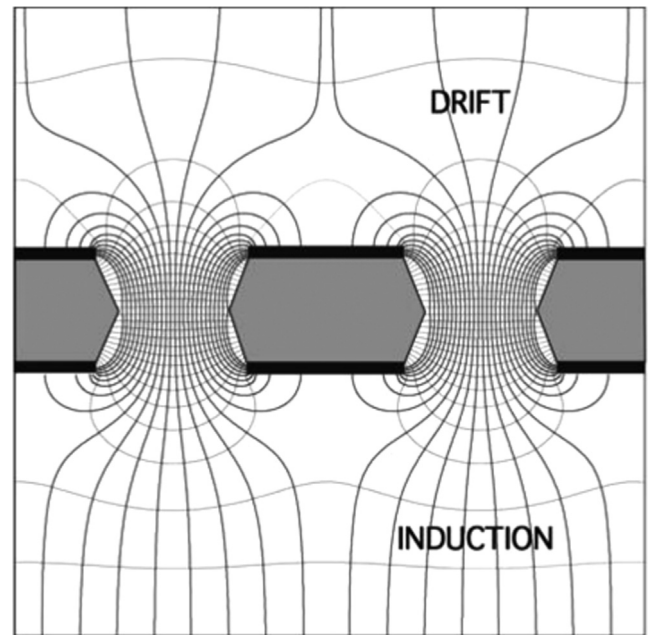


**Fig. 2.** Electric field in the region of the holes of a GEM electrode.

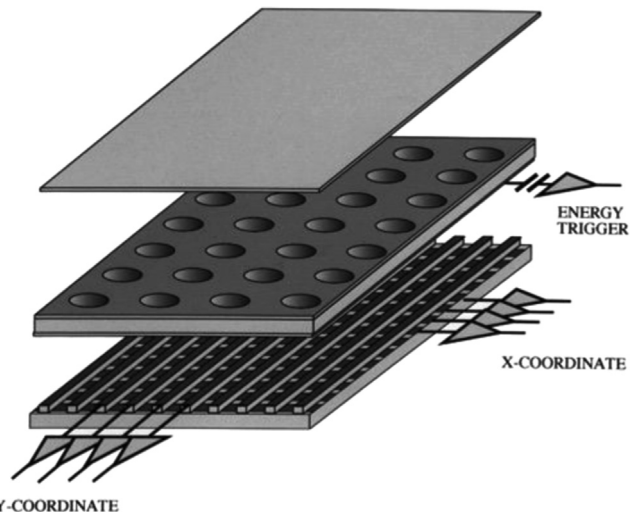


**Fig. 3.** Schematics of single GEM detector with Cartesian two-dimensional strip readout.

in early studies that to ensure high gains, the optimum hole diameter should be comparable to the foil thickness, as shown by the measurements in Fig. 4: while narrower holes result in larger fields for a given voltage, losses on the walls compensate for the increased gain [14]. It should be noted that, since a field-dependent fraction of the multiplying electrons is lost on the lower face of the GEM electrode, the useful or effective gain, defined as ratio of the detected to the primary ionization charge, is always lower than the real gain of the multiplier, as shown in the figure.

Owing to the structure of the detector, the sharing of collected charges (electrons and ions) between electrodes depends on the value of fields, GEM geometry and filling gas; it has been extensively studied both with measurements and simulations [14–17]. Fig. 5, from the first reference, is an example of currents measured on all electrodes as a function of the induction field, with all other fields kept constant. Above  $\sim 15 \text{ kV cm}^{-1}$ , avalanche multiplication begins in the induction gap; while exploitable to attain higher gains, this is not a desirable feature since it might help propagating a discharge through the structure.

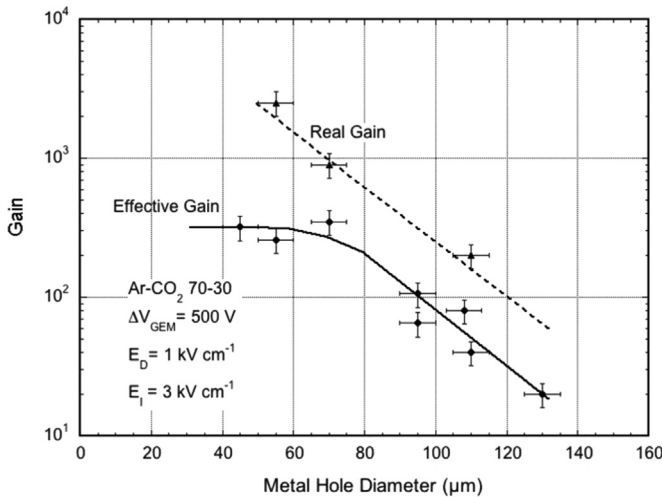


**Fig. 4.** Effective and real gain at fixed GEM voltage as a function of hole's diameter.

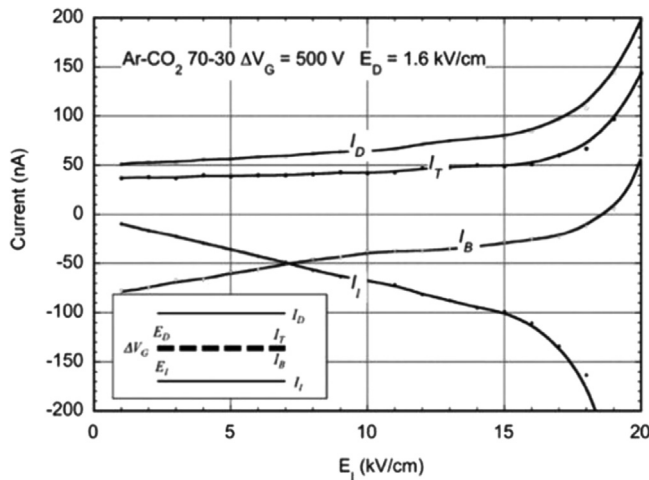


**Fig. 5.** Measured currents under irradiation on the four electrodes of a single-GEM detector, at increasing induction fields. Definitions are given in the inset.

The fraction of ionization electrons transferred through the GEM foil, or transparency, depends on the drift field, decreasing at high values due to losses to the top GEM electrode, as shown in Fig. 6, measured with a “standard” GEM geometry (70 μm holes at 140 μm pitch) and for other patterns, Fig. 7 [14]. Data are renormalized to take into account the increasing gain of the electrode with voltage. Interleaving of electrodes with different geometries in multi-GEM devices has been studied with the aim of reducing ion backflow in Time Projection Chambers, discussed in Section 12. Transparency losses are important in determining the energy resolution, and directly affect the efficiency of detection of single photoelectrons (see Section 13).

The maximum proportional amplification that can be attained before discharge depends on the GEM manufacturing quality, since a single local defect can affect the whole electrode. For small sizes and with thorough selection and testing of the electrodes, an effective gain well above 10<sup>3</sup> can be obtained, as shown in Fig. 8, measured in argon–carbon dioxide mixtures at atmospheric pressure. For larger areas this is rarely achieved, and it is preferred to adopt a multi-GEM structure to safely reach large amplification factors (Section 4).

The energy resolution achievable with GEM detectors compares with that of most proportional counters, ~17% FWHM for 5.9 keV X-rays, Fig. 9 [18]. Gain non-uniformities and shifts due to charging up of the insulator in the hole may degrade the resolution (see Section 6).

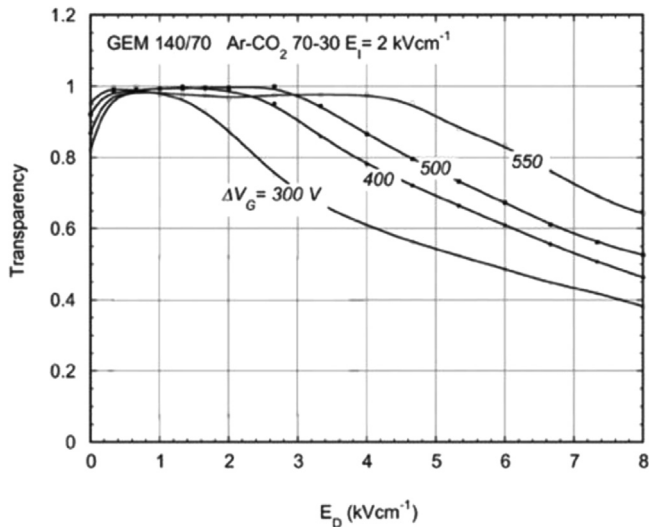


**Fig. 6.** Electron transparency of a standard GEM electrode (70 μm holes at 140 μm pitch) as a function of drift field for several values of GEM voltage.

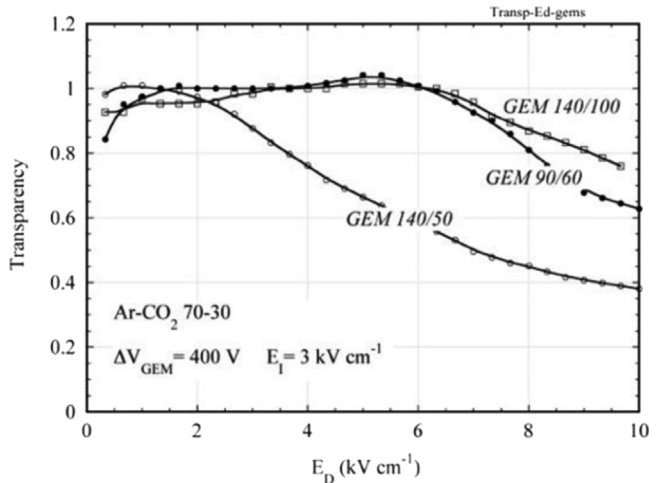


**Fig. 7.** Electron transparency for different GEM geometry, labeled as pitch/hole diameter.

GEM detectors have been operated successfully in a variety of gas mixtures and in a range of pressures, from a few torr to several atmospheres; examples will be given in the following sections. The device has also been operated at cryogenic conditions in dual-phase detectors (Section 15).

#### 4. Multi-GEM structures

As mentioned in Section 1, an unique feature of GEM devices is that, with an appropriate choice of the fields, the fraction of amplified electrons transferring to the gas gap following a first electrode can be injected and multiplied in a second foil, and yet again in a cascade of GEM electrodes [10,19,20]; structures of up to five multipliers have been successfully studied [21,22]. The noticeable advantage of multiple structures is that the overall gain needed for detection can be attained with each of the electrodes operated at much lower voltage, therefore much less prone to discharges; as discussed later, this has permitted to efficiently detect single electrons released in the gas by ultra-violet photons.

A Triple-GEM detector is shown schematically in Fig. 10. The result of thorough optimization studies aimed at realizing detectors with high rate capability and reliability, the device has three identical

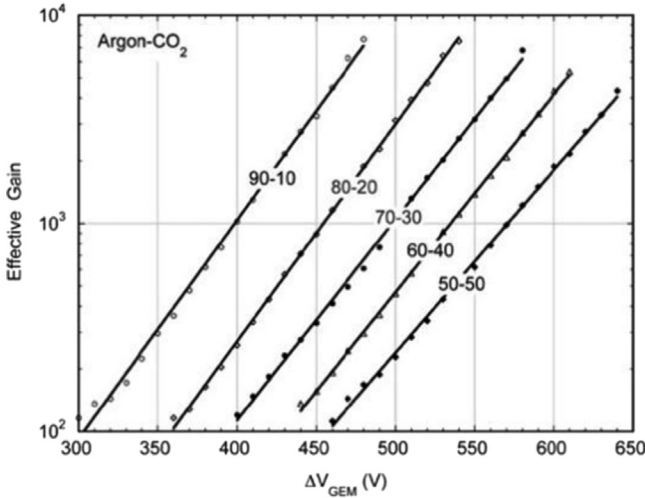


**Fig. 8.** Single GEM effective gain as a function of voltage in Ar-CO<sub>2</sub> mixtures at atmospheric pressure.

GEM electrodes and an anode separated by 2 mm gaps; the drift gap is 3 mm thick, to ensure efficient detection of minimum ionizing tracks. The drawing shows also the scheme used to distribute the appropriate voltages to all electrodes, a simple resistive chain with a single voltage source. Other powering schemes permitting to vary the individual voltages have been used during the developments and by other authors (see for example [23]).

While the final test of the reliability of a detector is its long-term use in realistic experimental conditions, a procedure has been established permitting the comparison of performances in the laboratory [24]. The detector is first characterized with an exposure to a moderate flux of soft X-rays (5.9 keV from an <sup>55</sup>Fe source); the effective gain is measured as a function of voltages, and the maximum safe operating voltage determined. The chamber is then exposed to a source releasing much larger ionization, and the discharge rate is determined at increasing values of voltage. A convenient source to this extent is the 6.4 MeV  $\alpha$  decay of <sup>220</sup>Rn, introduced with the gas flow from a natural thorium generator. Fig. 11 [25] shows a compilation of gain measurements and discharge rates with the internal  $\alpha$  source as a function of voltage applied to each electrode in the Single-, Double- and Triple-GEM configuration. Considering the onset of discharges as operating limit, a gain above  $10^4$  can be safely reached in the triple structure. While the radiation environment in an experiment differs from the laboratory conditions, the results can be taken as a guide-line for the design and comparison of detectors. Further studies have shown that a small asymmetry ( $\sim 10\%$ ) in the sharing of amplification between electrodes, with the first GEM in the cascade operated a slightly higher gain, increases the discharge immunity [25]. The amount of moisture in the gas also affects the results, and should be kept below  $\sim 50$  ppm [26].

The measurements described above have been performed with a 70-30 Ar-CO<sub>2</sub> gas filling at one bar, a cheap, non-flammable mixture convenient for use in large experimental systems. Many other gases have been investigated to meet special experimental requirements; only some examples are given here. Mixtures with carbon tetrafluoride increase the electron drift velocity, improving the detector time resolution, but require higher operating voltages (Fig. 12 [27]).

Large gains can be attained also in pure noble gases [28], owing to the confinement of the avalanches in the holes that prevent photon feedback problems; Fig. 13 shows an example of gains measured with a Triple-GEM detector in a range of noble gases and their mixtures [29]. This opens up the possibility to use the multiplier in photosensitive sealed detectors and in dual-phase devices, discussed in Sections 13 and 15.

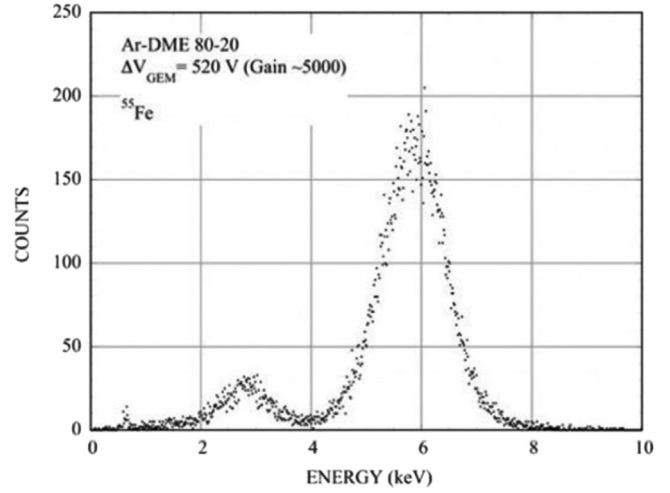


**Fig. 9.** Pulse height spectrum on 5.9 keV for a single GEM. The relative energy resolution is  $\sim 17\%$  FWHM.

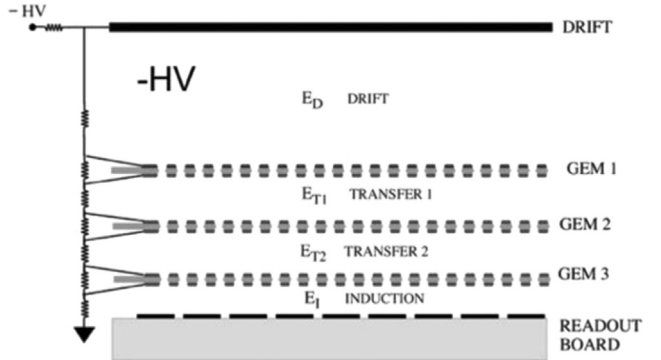


**Fig. 10.** Schematics of a Triple-GEM detector.

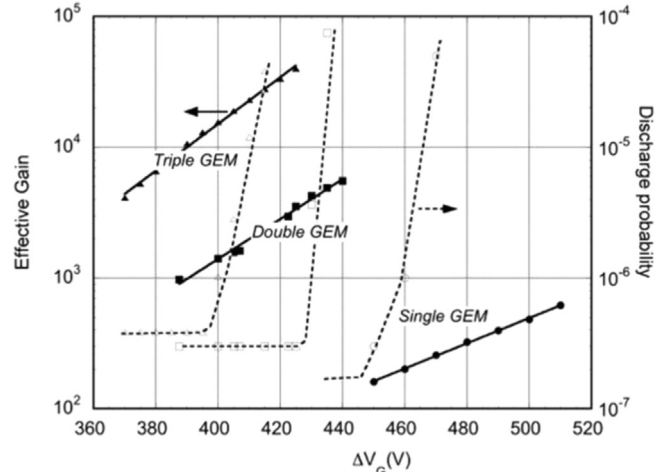


**Fig. 11.** Effective gain and discharge rates as a function of voltage in multi-GEM detectors.

The measurements described above were mostly realized at atmospheric pressures; for special applications, however, GEM detectors have been operated successfully at pressures between 10 and 50 Torr [30,31] and high pressure noble gases and their mixtures [32–35].

Originally motivated by the need of reducing the sparking probability in another micro-pattern device, Micromegas [36,37], use of resistive electrodes to locally quench the formation of discharges has been developed also for GEM-like detectors as an alternative to multiple cascaded electrodes [38–40]. As in similar

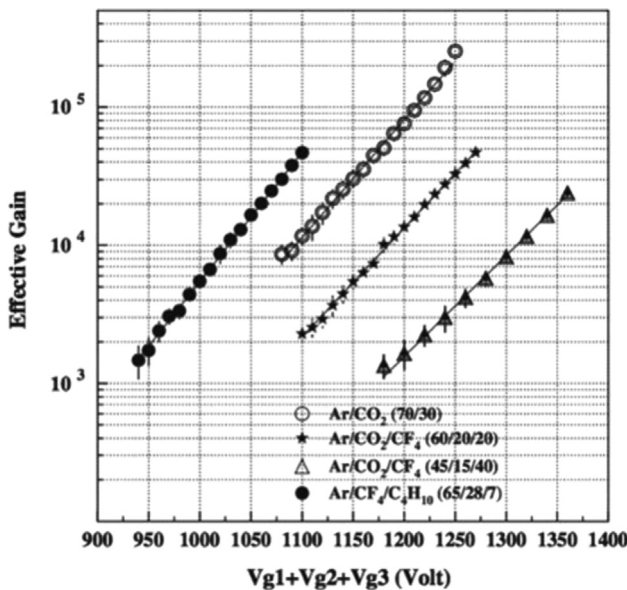


Fig. 12. Effective gain of a Triple-GEM detector in  $\text{CF}_4$  mixtures.

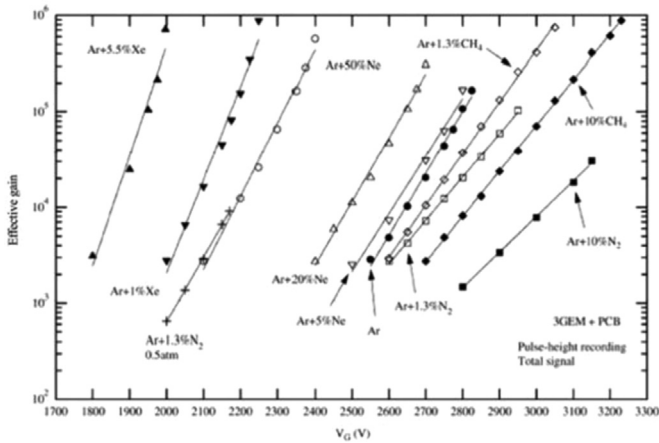


Fig. 13. Effective gain of a Triple-GEM in noble gas mixtures.

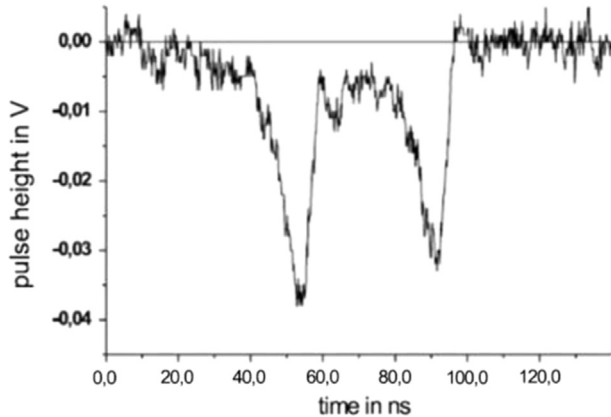


Fig. 14. Example of fast signals detected on the anode of a multi-GEM detector for two tracks close in time.

devices (resistive plate chambers and the likes), the technical issue is finding a suitable process for producing stable and well controlled layers of high resistivity; the local voltage drop induced by the detected current affects also the efficient operation of the detectors at high radiation fluxes [41].

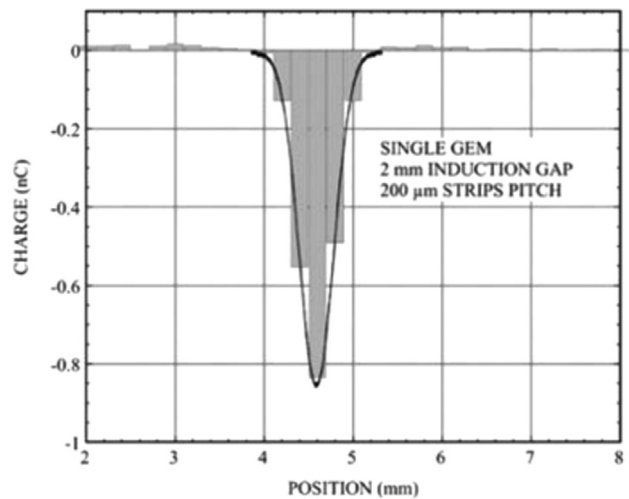


Fig. 15. Induced signals profile recorded on parallel anodic strips at 200  $\mu\text{m}$  pitch.

## 5. Signal formation

The amplified charges (electrons and ions) resulting from the multiplication process are collected on the various electrodes, in field-dependent relative proportions; Fig. 5 provided a representative example. The anode, last electrode in the structure, only gathers the electrons leaving the last GEM; the induced negative signal is therefore very fast, as it corresponds to the drift of the high mobility electrons over a few mm. Fig. 14 gives an example of pulses detected with a fast current amplifier on the anode; one can disentangle two tracks separated by less than  $\sim 20$  ns. In a drift or time projection chamber this would correspond to about one mm multi-track resolution. As shown in Fig. 3, the anode can be patterned with one- or two-dimensional projective readout strips to perform localization. For a single GEM and a localized event (a soft X-ray conversion) Fig. 15 shows the profile of recorded charge on a set of parallel readout strips, 200  $\mu\text{m}$  apart; the FWHM of the distribution is about 600  $\mu\text{m}$ , and the corresponding two-track resolution better than a mm [42].

It should be noted that the signal induction is caused by the motion of the electrons towards the electrode; as shown in Fig. 16, from the previous reference, while the strips facing the event collect a charge proportional to the avalanche spread, strips on the side detect a positive signal but no integral charge, as it can be inferred by simple electrostatic considerations (see for example Section 6 of Ref. [2]).

A signal identical but of opposite polarity is induced by the electrons collection on the bottom GEM electrode, facing the anode, and can be used to generate an energy trigger permitting the synchronous recording of the anode signals for neutral radiation. However, because of the large capacitance of the foil, the requirements on the amplifiers are more stringent than for the anodic strips. Also, owing to the capacitance between GEM and facing electrodes, a fraction of the positive signal is induced on the anode, generally negligible for narrow strips but that may become important if large areas of the anode are interconnected. A decoupling capacitor added to the GEM electrode may be used to cancel the fast positive component of the pulse.

The width of the induced signal profile depends on many factors: the extension of the primary ionization trail released in the drift gap, the number and distance of the GEM electrodes, the gas-dependent diffusion of electrons during the avalanche and transfer processes.

Positive ions created in the multiplication process are partly collected by the electrodes, with a fraction slowly receding into

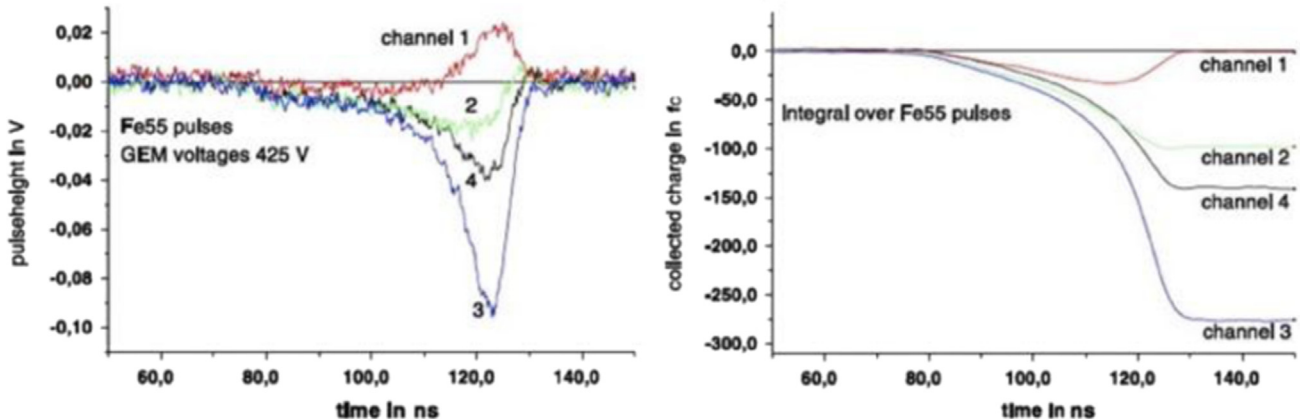


Fig. 16. Fast induced charge (left) and integrated charge on adjacent anodic strips, 500  $\mu\text{m}$  apart, for an event localized on strip #2.

the drift gap. Defined as ion backflow, the ratio of positive ions reaching the drift electrode to the electron charge detected at the anode has been extensively studied with the aim of reducing the field distortions in large volume drift and time projection chambers (Section 9).

## 6. Manufacturing of GEM electrodes

The early GEM electrodes were produced using a double-mask, high-quality wet etching technique. The production starts with the procurement of a high-quality polymer foil coated on both sides with a thin metal layer (in most cases, 50  $\mu\text{m}$  thick kapton with 5  $\mu\text{m}$  copper). The manufacturing method<sup>1</sup> shown schematically in Fig. 17, left, requires the exposure of the metallized polymer foils, coated with a photosensitive resin, to ultra-violet light through masks from both sides of the sheet. Once the metal is chemically removed following the hole's pattern, the foil is immersed in a solvent for the polymer until holes dig in from the two sides, resulting in a characteristic double-conical shape (Fig. 18 [26]). To satisfy the stringent requirements on diameter and pitch of the holes, the two masks have to be aligned with a tolerance of a few microns, an increasingly tough requisite for large sizes. Fig. 19 shows the author holding one of the GEMs built for the COMPASS tracker; several hundred foils of this design have been built at CERN.

A single mask process has been refined to achieve the realization of larger areas, up to and above a square meter, Fig. 17 right [43]. Following the masking, metal and polyimide etching, the foil is chemically etched to remove about half of the metal, opening the holes on the bottom side; a second polyimide etching permits one to realize quasi-conical holes (Fig. 20 [44]).

The detailed shape of the holes plays an important role in determining the detector performances: the double-conical shape permits one to reach high gains but shows a slow gain increase at startup due to charging-up of the insulating surfaces during operation. In contrast, a cylindrical shape offers a more stable operation, but is more prone to discharges at high gains [45]. A comparison of the time-dependent relative gain shift for three shapes of the holes (cylindrical, conical and double-conical) is shown in Fig. 21 [45]. Differences may also emerge between electrodes seemingly identical but produced by different manufacturer [46].

Alternative production methods have also been developed, such as plasma etching [47] and laser drilling [48]: mechanical

drilling of thicker supports, used for the manufacturing of the optimized [49], thick [50] or large electron multiplier (LEM) [51], suitable for applications requiring rigid electrodes, as photo-sensitive detectors or cryogenic devices. Fig. 22 shows A. Breskin with an early Thick-GEM. This development has been pursued in view of an application in Cherenkov Ring Imaging (see Section 13); Fig. 23 is cross-section through a mechanically drilled, one mm thick fiberglass sheet with 300  $\mu\text{m}$  holes at one mm pitch [52]. Other groups have developed technologies to produce hole patterns on a variety of supports [53–57].

In the Thick-GEM, the retreat of the metal from the hole, or rim, can be controlled by wet etching after the drilling of the holes, and has a clear impact on the amplification process; as seen in Fig. 24, a large rim favors large gains, but results in large gain shifts under irradiation due to the charging up of the insulating surface.

For digital tracking detectors, a moderate gain shift reaching saturation after short irradiation times is generally not a problem, and the double-conical geometry is preferred; the stability requirements are more stringent for devices aiming at the measurement of the energy loss of charged particles or neutral radiation. The gain shifts due to charging up of the insulators have been extensively studied with computer models [16,58].

Paramount for the construction of reliable detectors is the setting up of thorough test protocols for the GEM foils all along the manufacturing process. Simple optical inspection was used in the early productions; more sophisticated quality assurance systems have been developed, coupling digital imaging to a computer-based pattern recognition process. Together with a measurement of the hole's size and distance, the software can identify various kinds of defects, allowing to select good quality electrodes [59–63].

## 7. Detectors construction

The early GEM-based detectors, and still many medium-size devices, were realized mounting framed GEM foils within containment vessels built with fiberglass frames, rubber joints and bolts. Fig. 25 is a typical assembly, with the top frame removed, showing the high voltage feed-through and the printed board used to extract the signals, in this case a two-dimensional strip readout [20]. The assembled detector is operated in an open gas flow at atmospheric pressure.

Not taking part in the amplification process, and usually at ground potential, the anode can be patterned at will depending on the experimental requirements. Fig. 26 shows a two-dimensional projective readout with perpendicular strips at 400  $\mu\text{m}$  pitch. The electrode is manufactured with a technology similar to the one

<sup>1</sup> Processes developed by Rui de Oliveira and collaborators, CERN Detector Technologies.

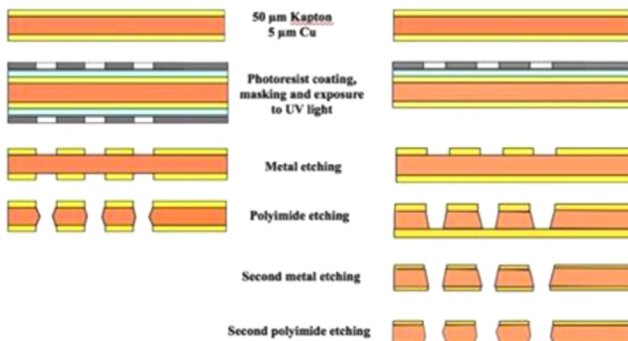


**Fig. 17.** Double- (left) and single-mask GEM manufacturing.

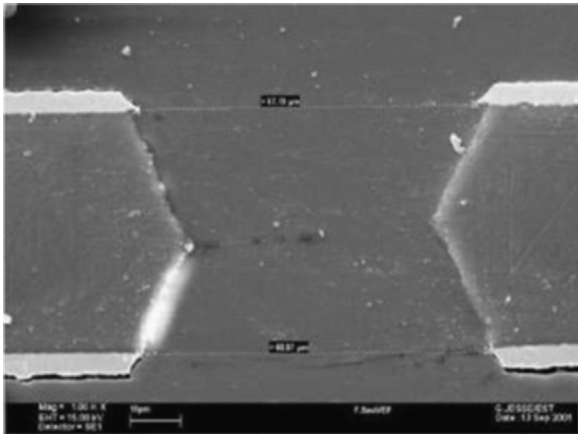


**Fig. 18.** Cross-section of a double-conical hole,  $\sim 70 \mu\text{m}$  in diameter at the surface, manufactured with two-masks wet etching.

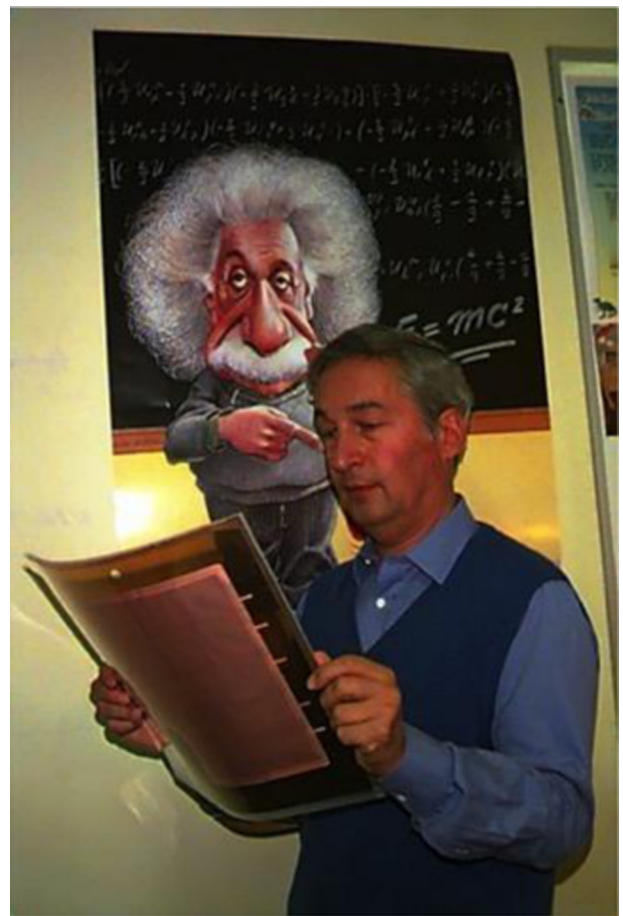


**Fig. 19.** The author holding one of the GEMs built for the COMPASS tracker.

used for the GEMs; a thin polyimide foil with engraved metal strips on each side is pasted on an insulating support and etched to remove the polymer between the upper layer of strips. To provide induced signals of comparable size on the two projections, strips have a different width in order to compensate for the screening effect of the top layer.

To reduce costs and the material budget, an all-glued light detector assembly has been developed for the construction first large GEM-based tracking system in CERN's COMPASS experiment. As shown in Fig. 27, the basic constituents are two light honeycomb plates on each side of the detector, ensuring mechanical rigidity and gas tightness; the internal components: GEM foils, readout and drift electrode are stretched and glued to thin insulating frames in sequence [26]. The assembly is very light ( $\sim 0.7\%$  of a radiation length in the active area), an essential requirement for a spectrometer.

To avoid the deformations caused by electrostatic attraction between the foils, spacer frames with thin insulating ribs are inserted in all gaps (Fig. 28). Fig. 29 shows one of the chambers during construction, enclosed in a nitrogen-filled box for HV testing. More than 20 detectors of this design, with  $30 \times 30 \text{ cm}^2$  sensitive area, have been built and successfully used for many years [64]; they are still operational at the time of writing.

Although infrequent thanks to the optimization work described above, occasional discharges may be induced during operation, particularly in high intensity beams. It was found experimentally that to prevent damages the area of the electrode should be smaller than  $\sim 100 \text{ cm}^2$ , limiting the stored energy [25]. For large area GEMs, this can be ensured "sectoring" the electrodes, with individual high value protection resistors, visible in Fig. 29. Moreover, in case of local defects, a sector can be externally disabled preserving the

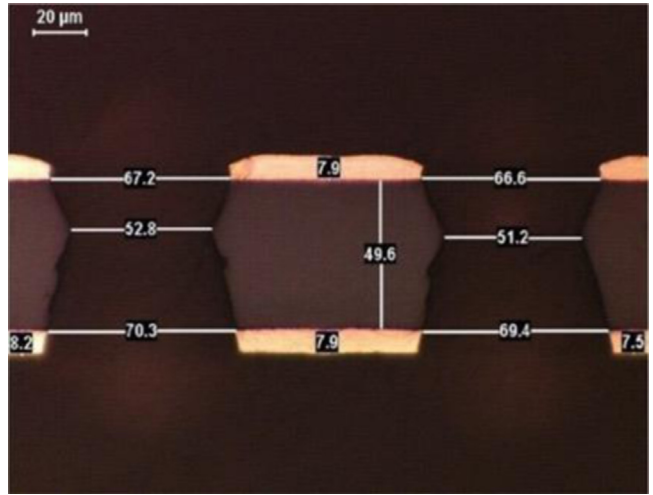


**Fig. 20.** Cross-section of a quasi-cylindrical hole,  $\sim 60 \mu\text{m}$  in diameter, made with single mask wet etching.

functionality of the remaining area of the detector. In the COMPASS design, an independently powered central circular sector (the beam killer) permits one to inhibit the beam area for high intensity runs.

Built with a similar design but different geometry, the half-moon shaped GEMs of the TOTEM tracker, Fig. 30, illustrate the great flexibility of the technology; Fig. 31 shows one of the four segments of the tracker, with 10 semi-circular GEM chambers and front-end readout electronics [65].

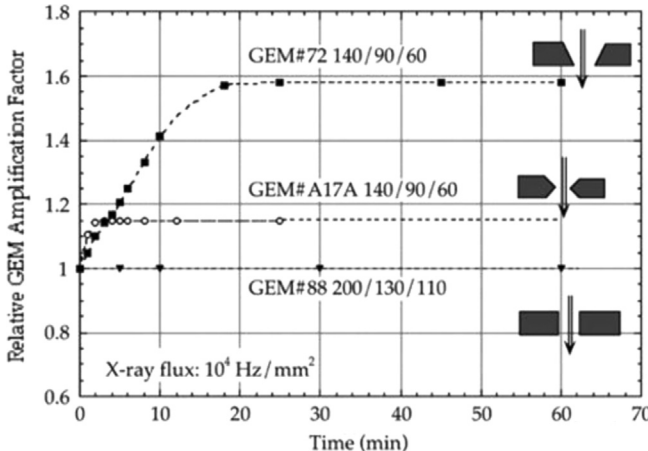


**Fig. 21.** Relative gain shift as a function of time at fixed radiation flux for three shapes of the GEM holes, indicated in the insets.

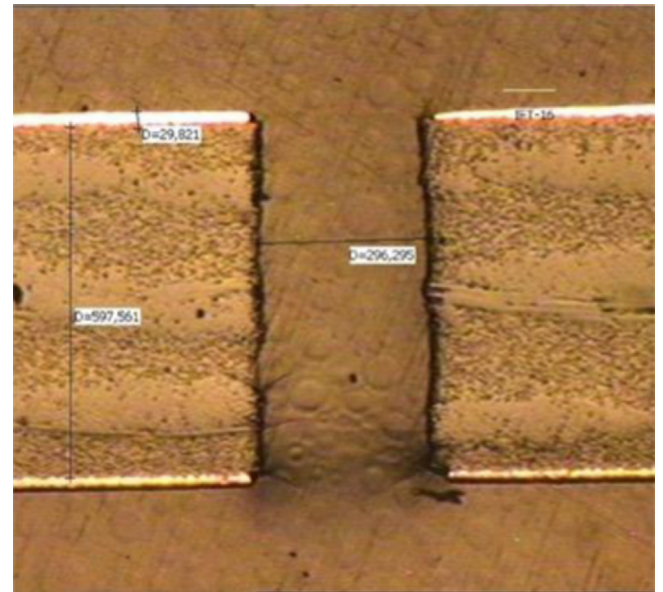


**Fig. 23.** Cross-section through a 300  $\mu\text{m}$  diameter hole of the Thick-GEM.



**Fig. 22.** A. Breskin with a medium-size Thick-GEM.

For large area detectors, the projective strip readout results in signals pile up at high particle rates. GEM detectors with a readout pattern having  $32 \times 32$  pads,  $1 \text{ mm}^2$  each in the beam region and X-Y strips covering the outer area have been built for the COMPASS upgrade, and operate efficiently up to particle fluxes exceeding  $10^5 \text{ Hz mm}^{-2}$  [66].

The described all-glued assembly is not suitable for the construction of large size devices, where replacement of a defective component should be envisaged. Named self-stretching, a dismountable assembly scheme developed for the upgrade of the CMS forward muon detector at CERN is shown in Fig. 32 [67]; the GEM foils are kept by a set of pins at the edges onto a frame that can be stretched from outside the structure, ensuring a mechanical tension sufficient to avoid electrostatic distortions without the use of internal spacers. In case of problems, the detector can be disassembled for inspection and replacements. Fig. 33 shows one of the prototypes during construction, about one meter on the long side. The GEM electrodes were manufactured with the improved single-mask technology, developed at CERN [43,44,68]. The detectors have been extensively tested in beam exposures, Fig. 34 [69,70].

## 8. Cylindrical GEM detectors

The flexibility of the GEM electrodes allows one to realize non-planar detectors, stretching the foils on a mandrel and pasting the electrodes over curved supports; a set of semi-cylindrical GEMs developed in the author's laboratory before assembly is shown in Fig. 35. Fig. 36 shows a radial Time Projection Chamber used in the BoNuS experiment: a cylindrical gas volume with radial electric field surrounds the beam target region; ionization electrons are drifted towards a set of semi-cylindrical GEMs amplifying the charge, detected on pad arrays on the outer surface [71].

The four-layer tracker for the KLOE upgrade is shown in Fig. 37 [72]; each layer has a cylindrical Triple-GEM detector, with the readout planes patterned with longitudinal and inclined strips. Tested in a solenoidal magnetic field up to 1.4 T, the detector provides a localization accuracy of 200 and 400  $\mu\text{m}$  rms for azimuthal and longitudinal coordinates, respectively.

## 9. Detection and localization of charged particles

GEM detectors were originally developed to achieve high rate, high accuracy detection and localization of fast charged particles in High Energy Physics. Owing to their versatility, they have also been used in a variety of other applications requiring detection of charged and neutral radiation; some will be discussed in the following sections.

Fast, singly charged particles release, in a 3 mm drift gap filled with argon-based mixtures at one bar, around 30 electron-ion pairs. With a Triple-GEM operated at an effective gain of  $10^4$ , this results in a detected charge on the anode of  $\sim 3 \times 10^5$  electrons, or  $\sim 5 \text{ pC}$ . For a 2-D readout scheme, recording the induced signal distribution on sets of parallel strips, this charge is shared between the two coordinates, and then again between several adjacent strips, used for localization. For the 400  $\mu\text{m}$  strips pitch adopted by COMPASS, the average number of strips sharing the charge (or cluster size) is two. The detection efficiency is then determined by the ratio of the signal to the noise of the front-end electronics used to instrument the detector. An example of pulse height spectrum measured on one coordinate with the COMPASS detector, using the fast analog

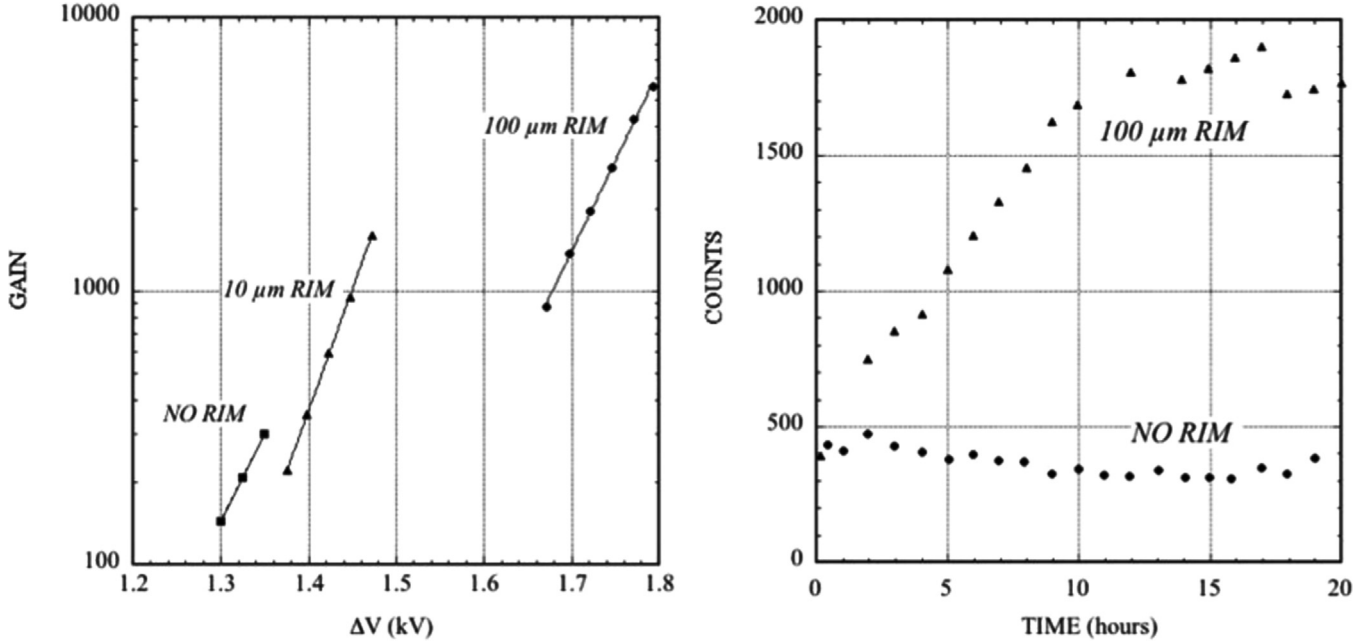


**Fig. 24.** Effect of the rim size on gain (left) and gain stability (right) for the Thick-GEM.

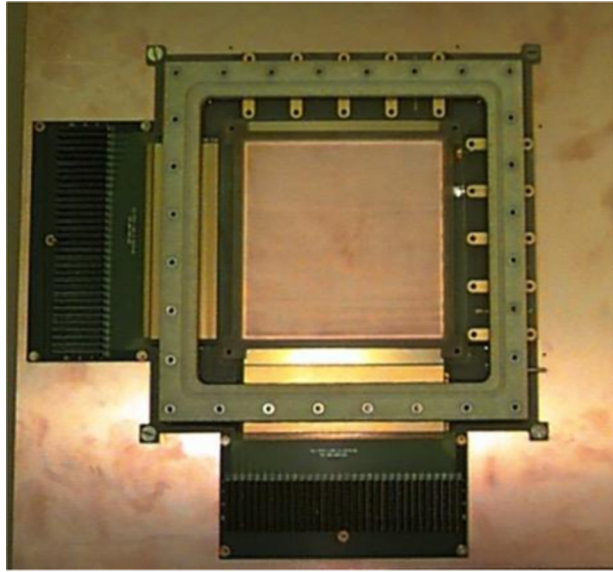


**Fig. 25.** A dismountable GEM detector assembly; the top frame (comprising the drift electrode and gas window) has been removed.

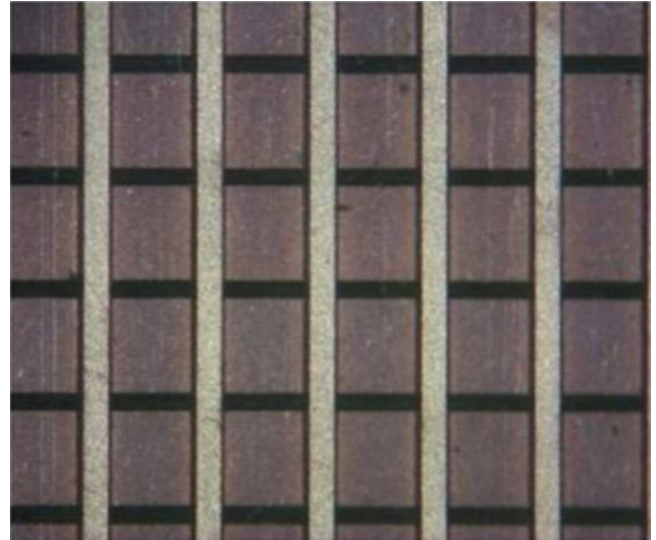


**Fig. 26.** Two-dimensional projective readout, with X-Y strips at 400  $\mu\text{m}$  pitch. Top and bottom strips are 80  $\mu\text{m}$  and 340  $\mu\text{m}$  wide, respectively.

The correlation between the X- and Y-coordinate charges, owing to the large energy loss spread typical for fast particles, permits one to resolve reconstruction ambiguities for multi-track events [26].

When using digital threshold discriminators for the front-end electronics, as for example the VFAT circuit implemented for the TOTEM detector [75], the position accuracy corresponds of course to the strips' pitch.

Convenient because of non-flammability and chemical stability, gas mixtures of argon and carbon dioxide result in moderate time resolution due to the relatively small drift velocity of electrons. Faster mixtures obtained replacing CO<sub>2</sub> with various proportions of carbon tetrafluoride have been extensively tested and used in experimental setups; the faster gas provides a factor of two improvement, an essential advantage for the operation of the detector in a high rate environment and to resolve events generated in successive collisions at CERN's LHC, 25 ns apart [27]. The time resolution depends also on

APV25 circuit [73] to record the induced signals, is given in Fig. 38 [26]; a discrimination threshold set to about 1/20 of the peak value ensures a detection efficiency close to 100% (Fig. 39).

The analog recording on strips of the detected charge for each event, combined with a center-of-gravity calculation, allows to infer the track coordinates with an accuracy better than the strip width. Fig. 40 shows the distribution of residuals, the difference between predicted and measured coordinates in the COMPASS spectrometer; the width of the distribution, 80  $\mu\text{m}$  rms, corresponds to the single coordinate position accuracy in real beam conditions [74]. This value is to a large extent determined by dispersions intrinsic in the detection processes of fast charged particles; much better precisions are obtained with neutral radiation (see Sections 13 and 14).

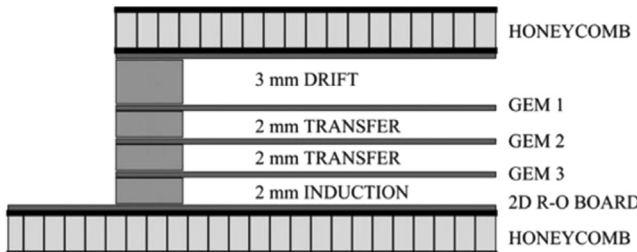


**Fig. 27.** Schematics of the COMPASS Triple-GEM detector.



**Fig. 28.** The thin insulating spacer used to prevent electrostatic deformations of the gaps. The central pattern corresponds to the beam area.

the value of the drift field as shown in Fig. 41 [76]. It should be noted however that the use of  $\text{CF}_4$  requires special precautions, because of the chemical reactivity of fluorinated compounds liberated in the avalanches in the presence of moisture [77], see also Section 10.

## 10. Rate capability and radiation resistance

In all gaseous counters, the positive ions generated in the avalanche process slowly recede to the negative electrodes until neutralized; the accumulated space charge modifies the electric fields, resulting in a reduction of gain above a certain value of radiation flux. In Multiwire Proportional Chambers, this limit is attained at around  $10^4$  particles per second per  $\text{mm}^2$  [3]. In GEM detectors, the capability is improved by several orders of magnitude thanks to the fast collection of most of the ions by the electrodes, and to the screening effect from external fields due to the confinement of the avalanches in the holes. As shown in Fig. 42, the proportional gain, measured on a single GEM exposed to a soft X-rays generator, remains constant up to a flux above  $10^6 \text{ s}^{-1} \text{ mm}^{-2}$  [45]. The measurement is performed in the counting mode for low and intermediate flux, while at the highest rates it is done in the current mode, matching the values at the transition.

A systematic study of rate dependence of gain in multi-GEM devices in a range of operating conditions and geometry has shown a tendency of the gain to increase at very high rates, probably due to space-charge field distortions; Fig. 43 is an example of measured gain as a function of rate for a Triple-GEM detector at increasing values of total effective gains (unpublished results from [78]). Simulation studies have attempted to reproduce this peculiar behavior [58]. These extreme rates are only met in special applications, as beam and soft X-rays plasma diagnostics, where gain uniformity is often not a major concern [79,80].

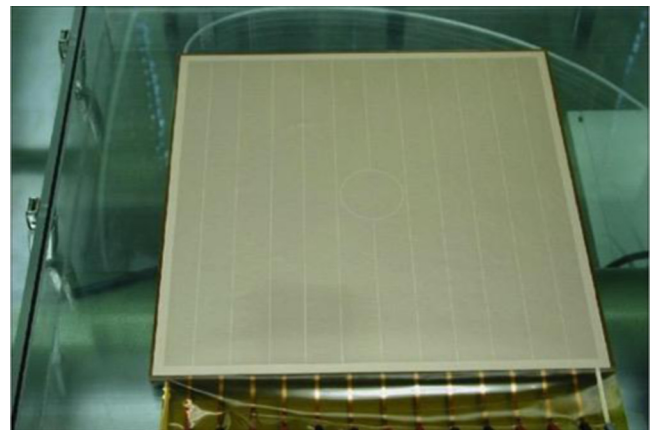


**Fig. 29.** A COMPASS Triple-GEM chamber under construction, showing the electrodes' sectored pattern.



**Fig. 30.** Half-moon shaped GEM for the TOTEM tracker.

Gaseous detectors under sustained irradiation can be affected by the so-called aging, a permanent damage resulting in a deterioration of performances. Discovered already in the early proportional and Geiger counters, the process has been extensively studied in view of the use of gaseous detectors in high radiation environments. The main cause of aging is the deposit on the electrodes of thin insulating layers resulting from the polymerization of organic gas molecules in the avalanche process; MWPCs, with their thin anode wires that are easily coated, are particularly affected. For a review of the aging processes see for example [2,4].

Motivated by the requirements of improving the time resolution (discussed in Section 9), the addition to the gas mixture of carbon tetrafluoride, owing to its well known etching properties, extends the detector lifetime up to and above a collected charge of  $20 \text{ C cm}^{-2}$  as shown by the measurement in Fig. 45 [27].

GEM structures, not relying on the field strength close to a thin electrode for amplification, are expected to have a reduced sensitivity to the presence of deposits; this has been verified experimentally with long-term irradiations, both in the laboratory and in experiments. Fig. 44 is an example of gain as a function of collected charge, measured with a Triple-GEM operated with an  $\text{Ar}-\text{CO}_2$  gas filling; no change is seen up to  $\sim 7 \text{ mC mm}^{-2}$ , Fig. 44 [81], corresponding at a gain around  $10^4$  to an integrated flux of  $\sim 2 \times 10^{13}$  minimum ionizing particles per

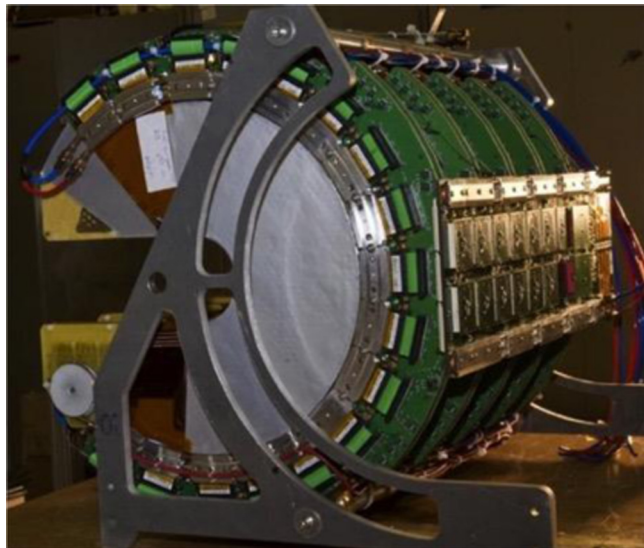


**Fig. 31.** One of the four segments of the TOTEM forward tracker, mounting 10 semi-circular Triple-GEM detectors.

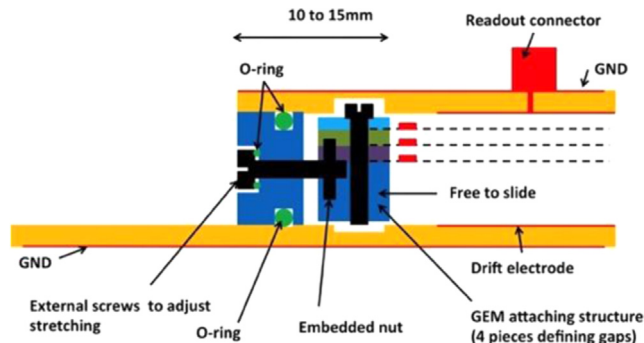


**Fig. 32.** The dismountable GEM assembly developed for the CMS muon detector upgrade.

cm<sup>2</sup>. In the development of the forward muon tracker for CMS, exposures to various fields of radiation have confirmed the long-term survivability of large GEM prototypes operated with CF<sub>4</sub> mixtures, Fig. 45 [76].

It should be noted that, while GEM devices are far more impervious to aging than other gaseous devices, gain drops have been sporadically observed during long-term operation, imputable to the penetration in the gas volume of silicon sealants improperly applied.<sup>2</sup> The use of CF<sub>4</sub> also requires special precautions, due to the reactivity of the fluorine liberated in the avalanches with water to form HF, one of the most aggressive acids for many materials [77].

## 11. GEM readout of time projection chambers

The excellent GEM multi-track resolution and the flexibility in the design of the anodic readout pattern have encouraged the development of GEM-based end-cap detectors for Time Projection Chambers, as replacement for conventional MWPC systems; the strong suppression of the ions backflow in the drift volume is an additional benefit, particularly for high rate-high multiplicity devices [82].

GEM-based TPC readout schemes have been developed in the framework of the International Linear Collider (ILC) studies [83,84].

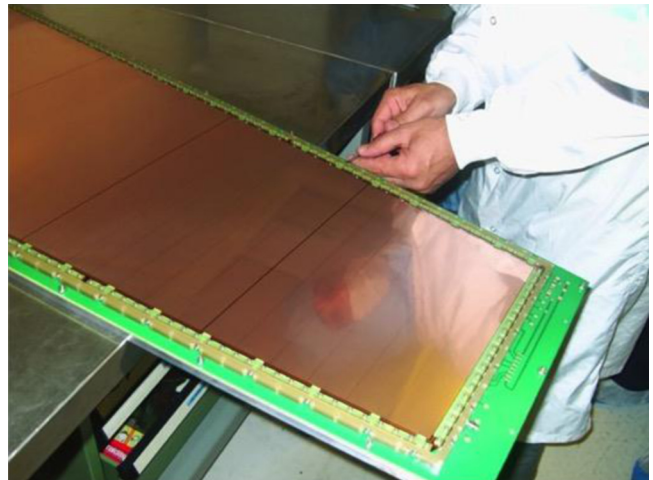


**Fig. 33.** A self-stretching Triple-GEM detector prototype for the CMS muon upgrade under construction.



**Fig. 34.** A large GEM prototype for the CMS forward muon upgrade. The detector is about one meter high.

Aiming at instrumenting large detection volumes, these works have focused on the optimization of the pattern and size of the readout pad rows, in order to minimize the number of electronics readout channels needed [85,86], and on the choice of the gas filling to satisfy the non-flammability, low diffusion requirements. Early

<sup>2</sup> B. Ketzer, personal communication at CERN.

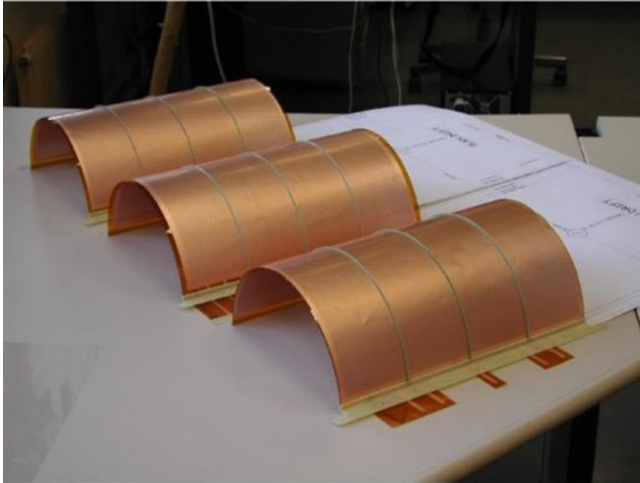


**Fig. 35.** A set of self-supporting cylindrical GEM electrodes.

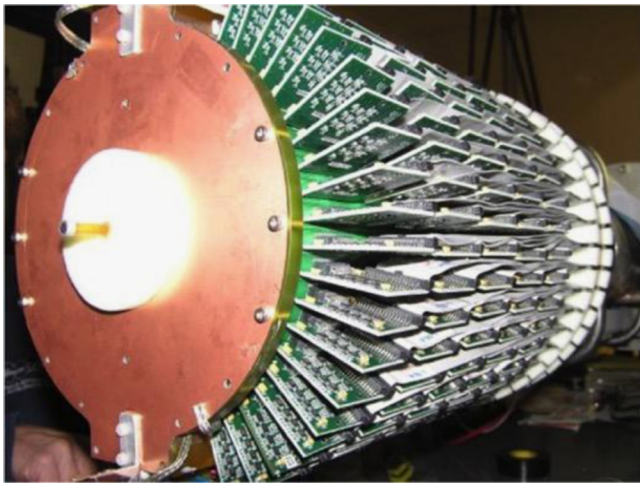


**Fig. 36.** The BoNuS radial TPC with GEM readout.

studies demonstrated that a few hundred microns spatial accuracy in a 4 T magnetic field could be attained in the so-called TDR gas (Ar–CH<sub>4</sub>–CO<sub>2</sub> in the proportions 93–5–2) [87,88].

Results of systematic measurements of transverse localization accuracy are shown in Fig. 46 for several values of magnetic field. The use of staggered pad rows (where the pads in every second row are shifted by half pitch) slightly improves the position accuracy [89].

Owing to their small electron diffusion, gas mixtures containing carbon tetrafluoride provide the best transverse space resolutions, Fig. 47 [90]; due to the higher drift velocity, the longitudinal resolution is instead worsened. Tempting also because of non-flammability and reduced sensitivity to background neutrons, CF<sub>4</sub>-based mixtures are however more difficult to use due to the higher voltage required for operation, as shown by a comparison of gain and discharge rate for a TPC with Triple-GEM readout for Ar–CH<sub>4</sub> and Ar–CF<sub>4</sub> (Fig. 48 [91]).

The appealing feature of the GEM readout, a narrow pad response function with substantial improvements in the multi-track resolution, implies the need of using large numbers of electronics channels. An elegant solution has been found coating the anode with a thin resistive layer between the induction gap and the readout strips or pads, thus widening the signal induction profile and providing good position accuracy with a reduced number of readout channels [92]. A center-of-gravity calculation of the charge distribution profile provides then an improved



**Fig. 37.** The Triple-GEM tracker for the KLOE experiment, 70 cm long.

transverse resolution as compared with a conventional readout, as shown in Fig. 49 [93]. Possible drawbacks of the approach are the difficulty to ensure a uniform response over large areas, due to variations of the added high-resistivity layer, and a reduced rate and multi-track resolution, caused by the long integration time of the signals.

In the framework of the design studies of the ALICE TPC upgrade, the medium size GEM-TPC systems FOPI [94] and PANDA [95] have been built and tested aiming at the optimization of the detector operating conditions, with a main emphasis devoted to the reduction of field distortions induced in the drift volume by the positive ions (see the next section): Fig. 50 shows schematically the FOPI detector, with an outer diameter of 30 cm and a drift length of 73 cm [96].

A promising line of development, probably reaching the ultimate tracking capability of gaseous devices, is the use of dedicated silicon pixel integrated circuits to collect the charge released in an overlying gas layer after amplification by a multiplying electrode, GEM or Micromegas [97,98]. Owing to the small capacitance of each pixel, the noise is very low (few hundred electrons) thus facilitating the detection of single ionization electrons with moderate amplifications. The simultaneous recording of charge and time on each pixel permits one to reconstruct events in a TPC-like device, with sub-mm resolutions. Fig. 51 is an example of a double track event recorded with the so-called GEMGrid, a hybrid detector realized by post-processing the Timepix silicon chip [99] with  $\sim 64,000$ ,  $55 \times 55 \mu\text{m}$  pixels to fabricate a GEM-like structure over a solid state pixel sensor; each dot represent the reconstructed 3-D position of a cluster in the ionization trails [100].

## 12. Positive ions backflow

As discussed in Section 5, in GEM structures the various electrodes collect electrons and/or ions produced in the avalanches in fractions that depend on the geometry, gas filling and applied fields. The final electrode (the anode) only collects the electrons generated by the last avalanches, while the first (the drift electrode) only collects ions. The fractional Ion Backflow (IBF), defined as the ratio between drift and anode currents, has been extensively studied in the development of large volume drift and Time Projection Chambers, since it induces strong field distortions<sup>3</sup> [101,102].

<sup>3</sup> Named also ion feedback, the process has also been studied in GEM detectors with semi-transparent or reflective photocathodes, where ions can damage the sensitive layers, see Section 14.

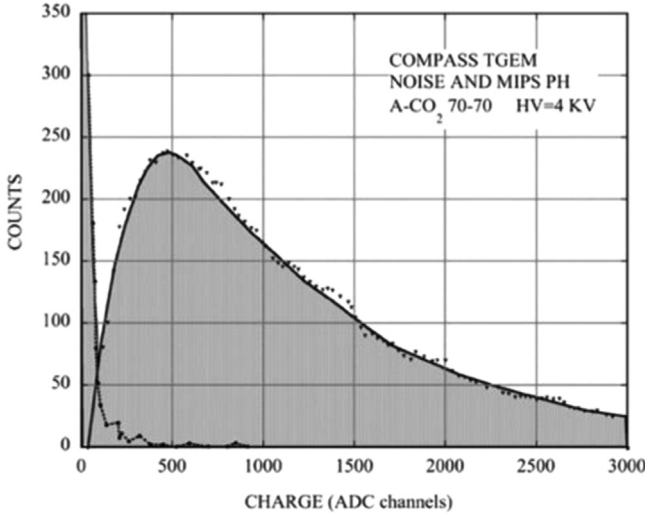


**Fig. 38.** Pulse height distribution measured for fast particles and electronic noise in the COMPASS GEM tracker.

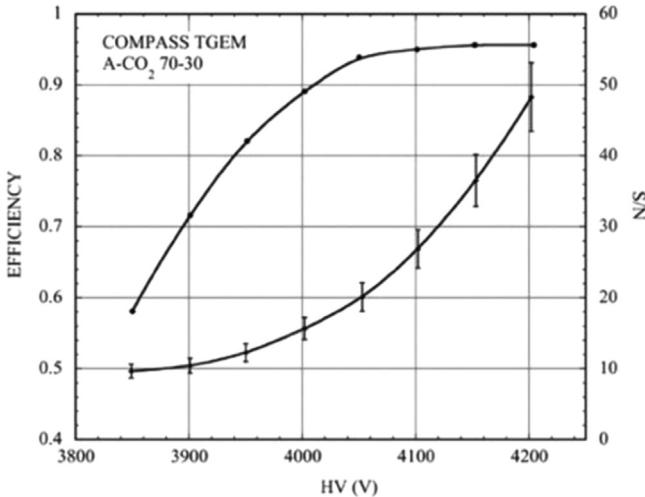


**Fig. 39.** Detection efficiency for fast particles and signal over noise as a function of operating voltage.

In the first generation TPCs, the IBF problem was avoided introducing an extra wire mesh in front of the active multiplier and applying a gating pulse synchronous with the beam interactions. This is still possible in some experiments (see later); in general however, the increase in collision rates make gating ineffective when the distance between events is shorter than the drift time. A lot of effort has been put therefore in exploiting the particular field configurations of single and multi-GEM devices to reduce the IBF in a continuous operating mode.

While for a single GEM the IBF is close to the ratio between drift and induction fields, in multiple structures a suitable sharing of the gains can substantially reduce its value. An example is given in Fig. 52, measured for a double GEM operated at an overall effective gain around  $10^4$  [14]; an asymmetric gain sharing reduces the direct IBF from the first multiplier. As can be seen, at the lowest drift field ensuring full electron collection ( $\sim 500 \text{ V cm}^{-1}$ ) the IBF is around 5%, a noticeable improvement over the ~30–40% observed using multiwire chambers for the readout [103].

Owing to the very different diffusion properties of electrons and ions, offsetting the holes in a pair of GEM electrodes results in

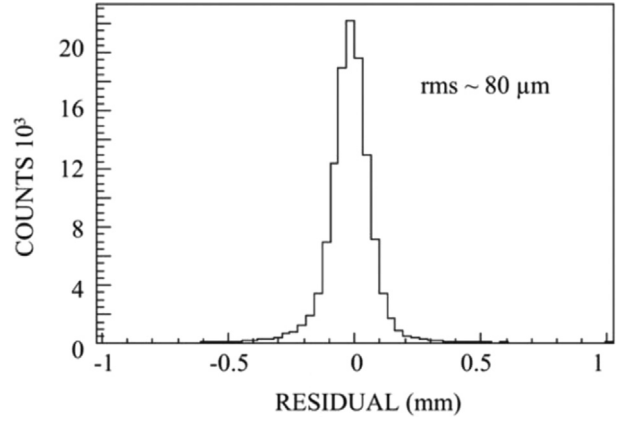


**Fig. 40.** Distribution of the position accuracy for fast particles.

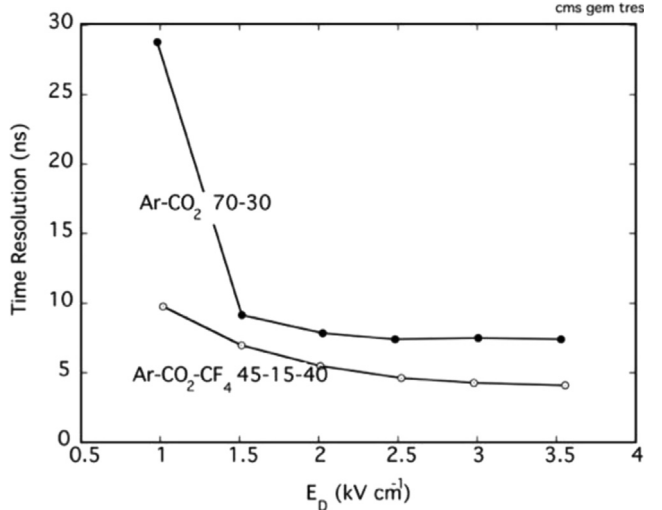


**Fig. 41.** Time resolution (rms) for fast particles measured with Ar-CO<sub>2</sub> and Ar-CO<sub>2</sub>-CF<sub>4</sub> gas fillings as a function of drift field.

a noticeable reduction of the backflow [102], an approach pursued for the design of the ALICE TPC upgrade.

The gain, gas and geometry dependence of IBF has been studied by many authors; Fig. 53 is an example, measured with a Triple-GEM having the hole diameter in the central electrode, 40 μm, narrower than those in the outer foils (85 μm) [21]. As it can be seen, the value decreases with the overall gain and is below 1% for high gain, low drift field. The choice of the operating parameters depends of course on other requirements of the experiment. Somewhat unexpectedly, the IBF is larger in gas mixtures where argon is replaced by neon or helium; reaching 0.8% in normal operating conditions in argon–CO<sub>2</sub>, it increases to 5% in neon–CO<sub>2</sub> [96]. This is presumably due to the lower fields needed for correct operation in lighter gases.

The IBF is reduced in a strong magnetic field parallel to the drift direction, probably because of an increased electron transmission due to the reduction of transverse diffusion; at 5 T, it reaches 0.2% (Fig. 54 [104]).

To achieve an IBF below 1% in neon-based gases, a four-GEM end cap detector has been developed for the ALICE TPC upgrade. It should be noted however that a reduction in the ion backflow may have as a consequence a loss of energy resolution, as seen in Fig. 55 [105]; a compromise is needed in detectors exploiting the measurement of energy loss for particle identification [106–108]. It has also been found, in systematic IBF studies, that the results

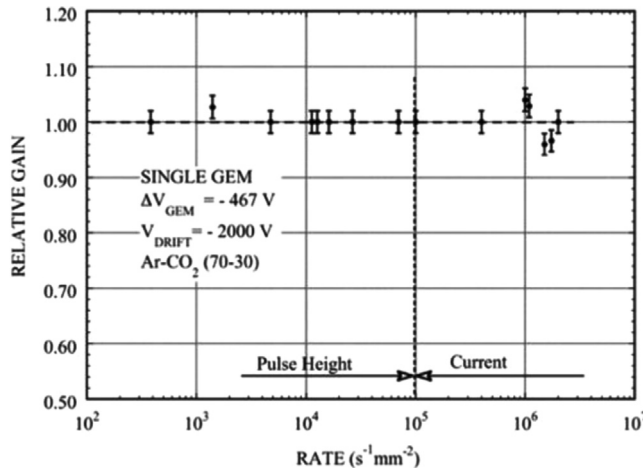


**Fig. 42.** Relative gain as a function of rate for a single GEM.

depend on the intensity of the source used for the measurement, with the tendency to be optimistic for surface charge densities above  $\sim 10^5$  fC cm<sup>-2</sup> [107]; this may explain discrepancies between results of different groups, as this parameter is often not quoted by the authors.

The process of ion accumulation in the TPC volume and ensuing field and electron drift trajectories modifications has been analyzed with the help of simulation programs; in principle this allows to correct the distortions [109,110]. However, its dynamic dependence from the source conditions (position, intensity and energy of the beams, etc.) make the correction process very laborious and computation intensive.

When acceptable in the experiment, the addition of a gating pulse can substantially reduce the IBF in large volume TPCs and consequently the distortions due to the accumulated space charge, as shown in a systematic study of a prototype GEM TPC with a gating grid for an experiment at J-PARC [91].

### 13. UV and visible photon detectors

In multi-GEM structures, very high gains can be attained in photosensitive gas mixtures containing a low ionization threshold vapor, owing to the effective suppression of photon feedback processes [111,112].

A more far-reaching development is to use semi-transparent CsI photosensitive layers deposited on the entrance window or on the GEM electrode itself. Large fields are required on the photocathode surface to efficiently extract the photoelectrons, due to the large back-scatter cross-sections of molecules; the effect is particularly relevant in noble gases, as shown by the quantum efficiency (QE) measured as a function of field at 185 nm for a semi-transparent CsI layer, relative to vacuum (Fig. 56 [113]). The highest QE values are obtained in carbon tetrafluoride and methane; recent measurements have shown that high efficiencies can also be reached for argon- and neon-methane mixtures [114].

A reflective photosensitive layer can be deposited on the first GEM electrode in a cascade, as shown schematically in Fig. 57 [115]. The reduction of the effective surface of the photocathode due to its optical transparency is compensated by the larger photoionization efficiency of thick reflective layers, also easier to manufacture as they do not require a strict thickness tolerance. With a proper choice of fields and geometry, electrons extracted by photoionization from the layer are efficiently dragged into the holes, where a first step of multiplication takes place. A low or inverted drift field prevents electrons released by ionizing tracks

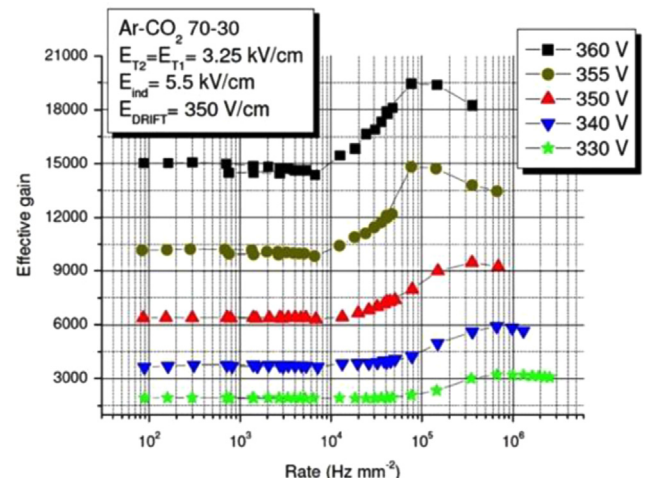


**Fig. 43.** Rate dependence of a Triple-GEM gain at increasing values of GEM voltages.

to be detected. Aside from the small dispersions caused by the avalanche development and diffusion the signals generated by photoelectrons in multi-GEM devices are isochronous; a time resolution of 1.6 ns rms has been achieved in a Quad-GEM with CF<sub>4</sub> gas filling [116].

Satisfying the high field requirement on the coated surface requires an optimization of the GEM geometry; Fig. 57 shows the photocurrent as a function of GEM voltage, measured in pure methane for CsI-coated GEMs of various designs. The best choice, the curve labeled dc100, corresponds to a GEM design with 100  $\mu$ m holes at 140  $\mu$ m distance [117] (Fig. 58).

The particular structure of a Multi-GEM detector, with relatively low fields in each element, results in exponential pulse height distributions for the signals generated by single electrons (Fig. 59 [115]) and does not allow in general to reach the Polya regime with the appearance of a peak.

The space and multi-hit resolution properties of a GEM detector with CsI reflective photocathode have been studied using a special anode readout pattern, named hexaboard, having a matrix of hexagonal pads interconnected at 500  $\mu$ m pitch through a multilayer printed circuit board to provide three projections at 120° for each detected photoelectron. Exposed to a collimated UV photon source, the device could emulate a multi-photon event, shown in Fig. 60; the single-photon position accuracy is around 55  $\mu$ m rms, with a two-photon resolution of around 200  $\mu$ m [118].

Much better position accuracies can be achieved using a solid state sensor as readout element, with active charge-collecting pads facing the gaseous multiplier; a calculation of the center-of-gravity of the detected charge profile gives a further improvement. In the course of development of the X-ray polarimeter (see the next section), and using a large scale integrated ASIC readout chip having ~22,000 hexagonal pixels, 50  $\mu$ m in diameter and a custom thin GEM foil with ~30  $\mu$ m holes at a 50  $\mu$ m pitch, an intrinsic position accuracy for UV photons of ~5  $\mu$ m rms has been demonstrated, as it can be inferred by the self-portrait image in Fig. 61 [119].

A first large scale application, an array of CsI-coated multi-GEM modules operated in the PHENIX experiment at the Relativistic Heavy Ion Collider (RHIC). Named Hadron Blind Detector (HBD), it detects the UV photons emitted by Cherenkov effect in a CF<sub>4</sub> radiator by electron-positron pairs, in a TPC-like structure with a reverse drift field to avoid detection of direct ionization (Fig. 62 [120]). Depending on the threshold set for the number of detected photoelectrons, hadron rejection factors above a hundred can be obtained.

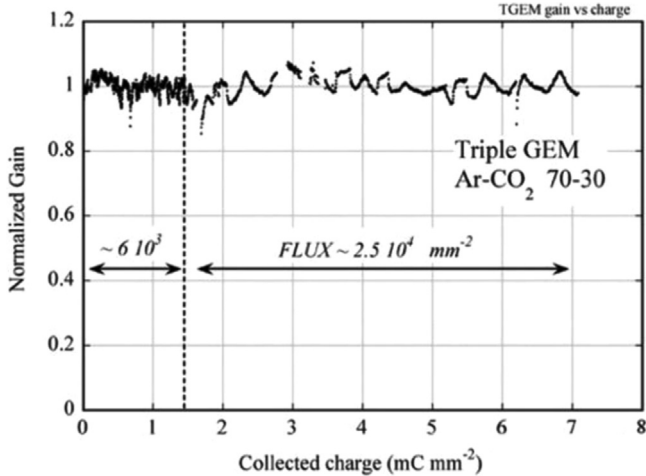


**Fig. 44.** Normalized gain as a function of collected charge in Ar-CO<sub>2</sub> (COMPASS Triple-GEM).

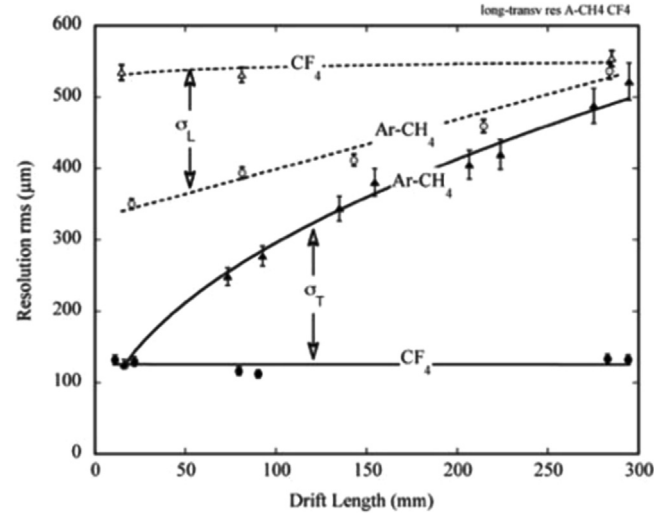


**Fig. 47.** Transverse (full curves) and longitudinal (dashed) resolutions measured with a GEM-TPC in argon-methane and carbon tetrafluoride gas fillings.

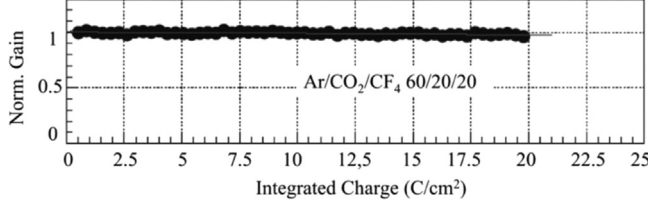


**Fig. 45.** Normalized gain as a function of integrated charge for the LHCb Triple-GEM detectors.

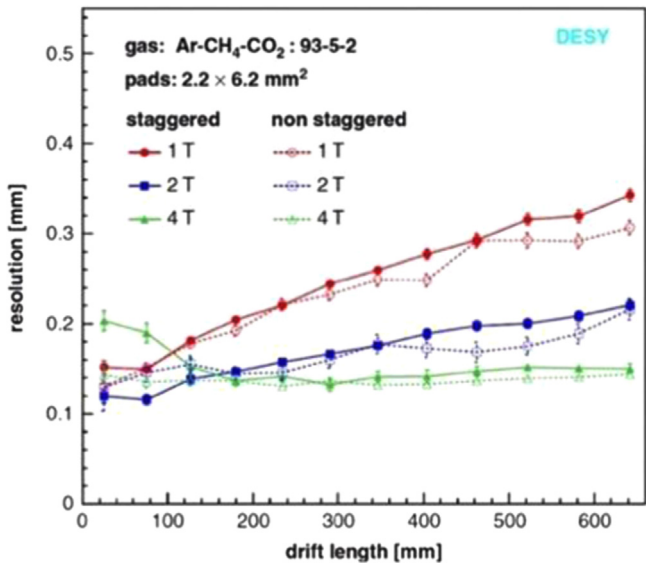


**Fig. 46.** GEM-TPC longitudinal resolution as a function of drift length and magnetic field.

One of the applications of UV-sensitive devices is for the method of particle identification exploiting Cherenkov Ring Imaging (RICH). Requiring the construction of large area CsI-coated GEMs, this application favors the use of Thick-GEM electrodes, sturdier and easier to handle than standard thin-foil electrodes. Originally implemented for the COMPASS RICH-1 upgrade with a single, high gain electrode [121], the instability problems discussed in Section 6 and the large ion backflow that could damage

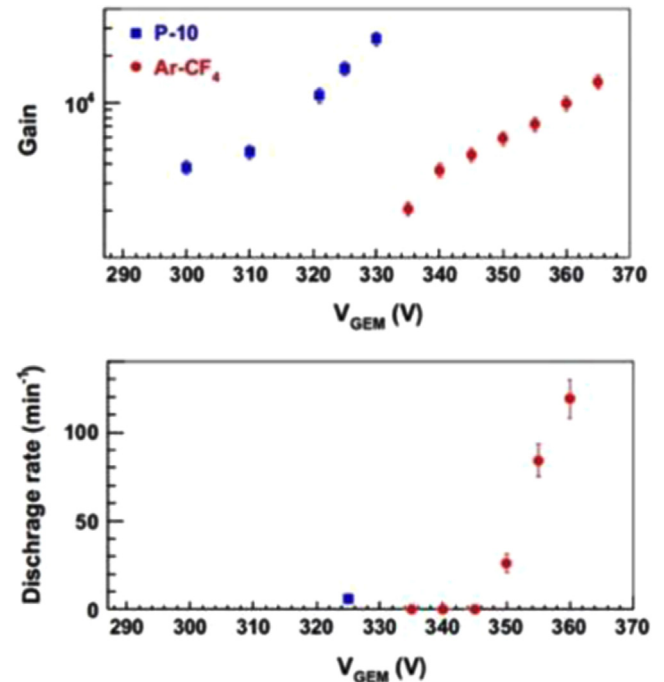


**Fig. 48.** Gain and discharge rate in a Triple-GEM TPC for Ar-CH<sub>4</sub> (P10) and Ar-CF<sub>4</sub> gas fillings.

the photosensitive layer led to the adoption of a multiple structure with misaligned holes, following [102]. With a Triple-Thick-GEM 30 × 30 cm<sup>2</sup> in size and a segmented anode readout on pads 12 × 12 cm<sup>2</sup> the group demonstrated the efficiency and localization properties of single photoelectron detection. Fig. 63 shows a multi-photon event with the reconstructed Cherenkov ring [122]. Similar developments are under way by other groups [55] [123].

Several attempts have been made to extend the spectral sensitivity of GEM detectors to the visible. This requires the deposition of multi-alkali photosensitive layers, extremely sensitive to contaminants, and implies the construction of sealed devices; moreover, the positive ions reaching the photocathode degrade the quantum efficiency after short irradiation times [124]. A big effort has been deployed to reduce the ion feedback with special patterning of the GEM electrodes; in the so-called Micro-

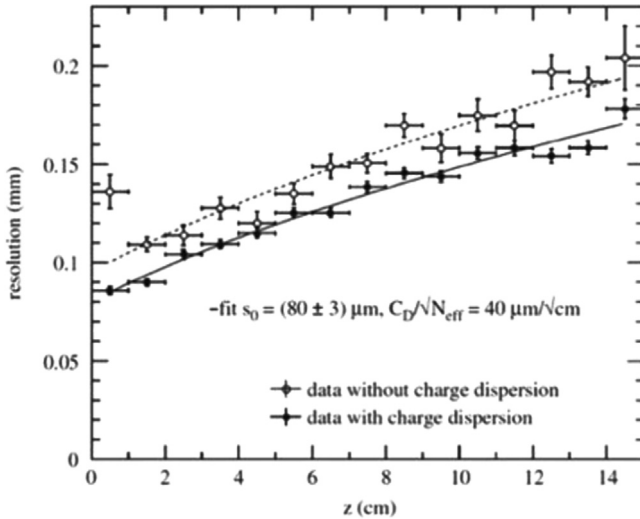


**Fig. 49.** Transverse position accuracy measured with direct and charge-dispersed readout.

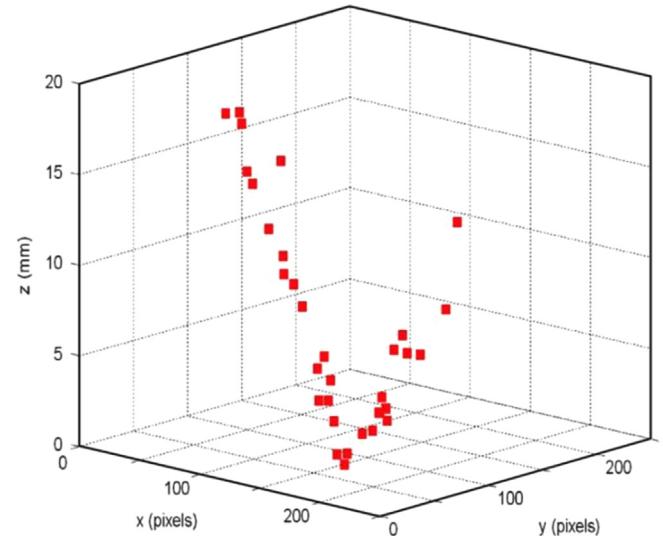


**Fig. 51.** A double track recorded with the GEMGrid detector. The pixels are 55  $\mu\text{m}$  on the side.

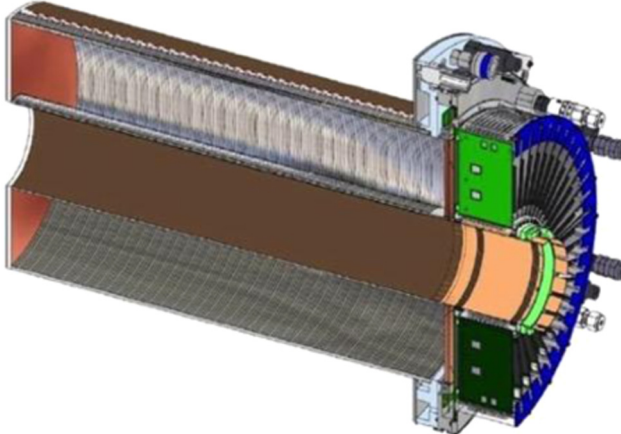


**Fig. 50.** The FOPI GEM-TPC detector.

Hole and Strips Plate, the addition of independently powered strips on the back side of a standard GEM permits one to reduce the IBF by an order of magnitude [125]. An even more complex micro-electrodes structures named COBRA reduces the feedback even further [126]. Despite the improvements, however, the residual ion current hitting the photocathode and the difficult manufacture of the structures has prevented so far a wide dissemination of the technology.

#### 14. Detection and localization of neutral radiation

The self-triggering capability, high rate performance and position resolution of GEM devices make them suitable as soft X-ray and neutron detectors; the moderate energy resolution, while forbidding spectroscopy applications, is appropriate for one-and two-dimensional imaging. A measurement of energy resolution at 5.9 keV was given in Fig. 9.

On exposure to a source, using the pulse detected on the lower electrode of the last GEM as energy trigger and recording the profile of detected charge on sets of anodic strips one can deduce the two-dimensional activity distributions with good spatial resolution. Fig. 64 is an example of soft X-ray absorption radiography of a small mammal; while of modest medical interest, the

image illustrates well the excellent contrast and resolution properties of the detector [18].

With argon-based gas fillings at atmospheric pressure, GEM detectors are efficient in the soft X-ray domain only below ten keV; higher pressures and/or xenon fillings extend the region of efficiency to higher energies. Systematic investigations of energy and position resolution have been described for a range of gases and operating conditions [127].

The very high rate capability of the detector consents to perform two-dimensional imaging of the X-ray emission for fusion plasma diagnostics; images of X-ray emission have been recorded with a pin-hole GEM camera on a matrix of readout pixels,  $2 \text{ mm}^2$  each at rates exceeding 4 MHz per pixel [128]. Further work has extended the test of the device to a mixed photon and neutron field as encountered around a fusion device; indeed, inherently to its design, the gas detector has a sensitivity to neutrons several orders of magnitude lower than for soft X-rays; Fig. 65 is an example of 2-dimensional image of the plasma source in the presence of an estimated neutron and gamma flux above  $10^6 \text{ s}^{-1}$  [128]. A similar device, using a Triple-GEM detector with one-dimensional projective strips readout has been developed to monitor the plasma radiation emitted by the Joint European Torus (JET) [129].

The flexibility in designing the shape of the GEM-based detectors is exploited also for wide-angle X-ray scattering studies. Following a concept introduced long ago to achieve high detection efficiency for energetic X-rays with gaseous detectors [130], the instrument has a radial drift and conversion gap where photons in the 8 keV range are converted without introducing a parallax error intrinsic in a planar device; a fan-shaped signal pickup electrode provides the coordinates along directions aiming at the scatter point. Sharing of the signals between several adjacent strips provides excellent radial localization accuracy, as shown in Fig. 66 [131].

The sub-mm imaging capability of GEM devices with solid-state pixel readout (see Section 13) has been exploited to measure the polarization of soft X-rays. As shown in Fig. 67, the recording and analysis of the ionization loss of an electron ejected by photoelectric effect permits one to identify the point of conversion and the direction of flight, thus providing the emission angle, perpendicular to the photon direction and to the plane of polarization [132].

The detection efficiency of gaseous counters drops rapidly at X-ray energies above 8–10 keV. Use of xenon or high pressures as gas fillings extends the sensitivity region, but increases the operating

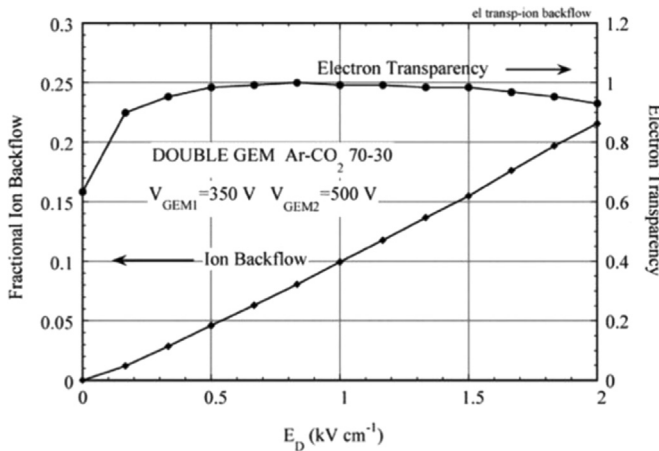


Fig. 52. Electron transparency and ion backflow in a double-GEM.

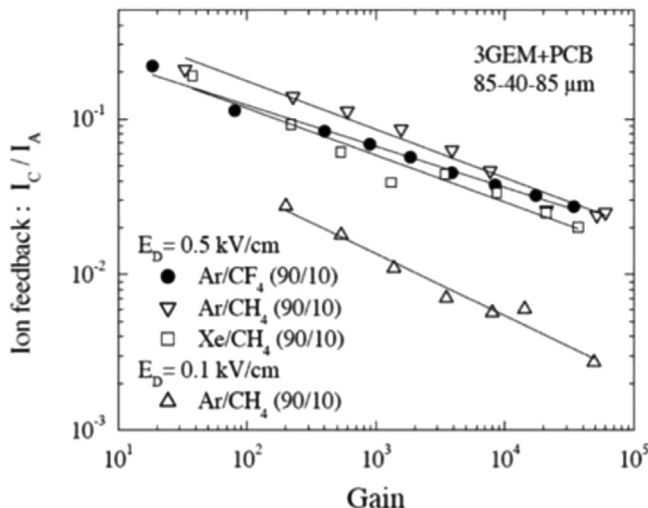


Fig. 53. Ion backflow fraction in a Triple-GEM as a function of gain and drift field.

difficulty. An effective solution to the problem is to use internal converters, thin high-Z layers where photons interact sending an electron into the active volume of the detector; the converter can be placed on the drift electrode or directly deposited on a GEM electrode. Fig. 68 shows a comparison of computed and measured detection efficiency as a function of photon energy for a detector using a gold-plated GEM foil as converter and first amplifier, followed by a cascade of three standard foils for full amplification; the efficiency can be increased with the use of multiple Au-coated GEMs in cascade [133]. A similar approach has been pursued in the development of high-rate hard X-ray detectors for portal imaging in medical diagnostics [134,135].

Filled with  ${}^3\text{He}$ , gaseous counters are used for detection of cold and thermal neutrons, exploiting the reaction  ${}^3\text{He} + \text{n} \rightarrow {}^3\text{H} + \text{p}$ , releasing in the gas a triton-proton pair. The ionizing yields can be amplified and detected electronically, or visualized through the light emission in the so-called optical imaging chambers (see Section 16). Confronted with the shortage of the helium isotope supplies, alternative devices making use of thin converter foils with high neutron cross-section have been developed. As for the detection of X- and  $\gamma$ -rays, the layers can be deposited on the cathode or directly on the GEM surface; multiple layers increase the detection efficiency. Ref. [136] gives a comparison of performances between gaseous and thin-foil converters in neutron detection. Owing to their design, GEM-based gaseous detectors

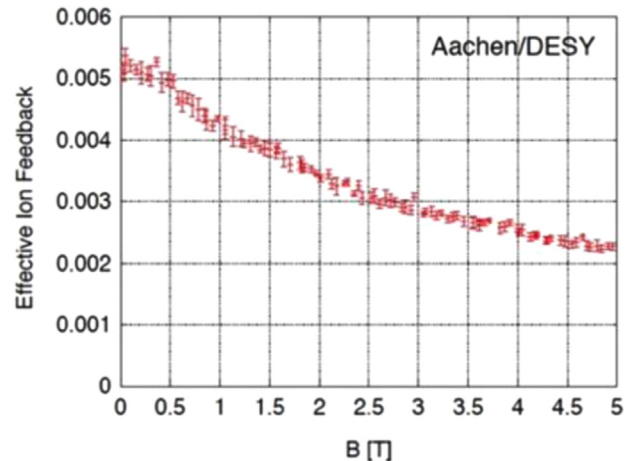


Fig. 54. Ion backflow in a Triple GEM at increasing values of magnetic field.

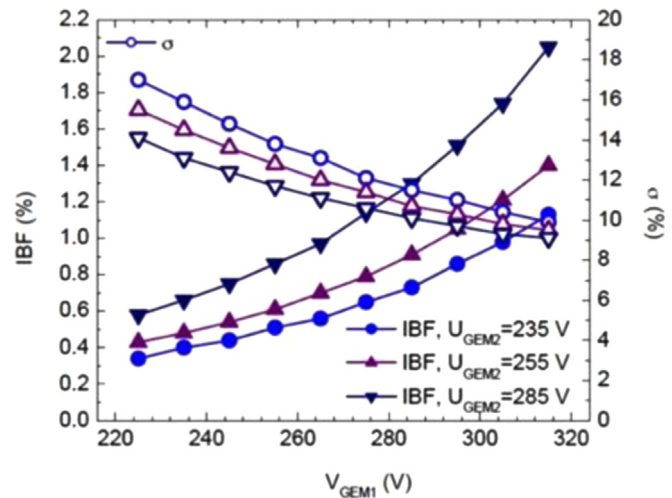


Fig. 55. Ion backflow and energy resolution as a function of voltage applied to the first of four GEMs in cascade.

have a very reduced sensitivity to the copious photon background present in most applications.

In the neutron detector CASCADE, a stack of  ${}^{10}\text{B}$ -coated GEM foils serve both the purpose of converter and charge amplifier; a symmetric assembly with a common central readout plane doubles the efficiency (Fig. 69 [137]). The detector, with an active area of  $200 \times 200 \text{ mm}^2$  has  $2 \times 128$  perpendicular signal pickup strips, read-out by dedicated ASIC chips recording the charge distribution for each event; a center-of-gravity algorithm then provides the position of the conversion with sub-mm accuracy. Fig. 70 is an example of the two-dimensional position distribution of a narrow neutron beam (0.57 mm in diameter) perpendicular to the detector, recorded at a neutron flux up to  $10^7 \text{ cm}^{-2} \text{ s}^{-1}$ .

Similar devices, making use of a Triple-GEM with a  $1 \mu\text{m}$  thick  $\text{B}_4\text{C}$  conversion layer deposited on the aluminum cathode, optimized for the detection of thermal neutrons, or a polypropylene and polyethylene converters suitable for fast neutron detection, have been extensively tested at the ISIS spallation source [138,139]. The devices can reach detection efficiencies of 1% and  $\sim 10^{-4}$  respectively for thermal and 3 MeV neutrons, and have very high rate capabilities.

The response of GEM devices for the detection of fast neutrons in thermonuclear fusion experiments has been studied both by simulation and measurements, particularly taking into account the heavy  $\gamma$  photons background characteristic of this operation [140].

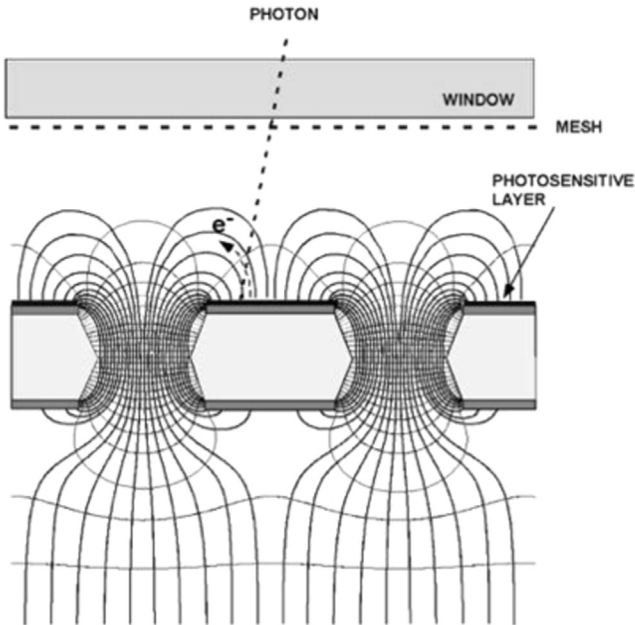


**Fig. 56.** A GEM electrode with reflective CsI photosensitive layer deposited on the upper face.

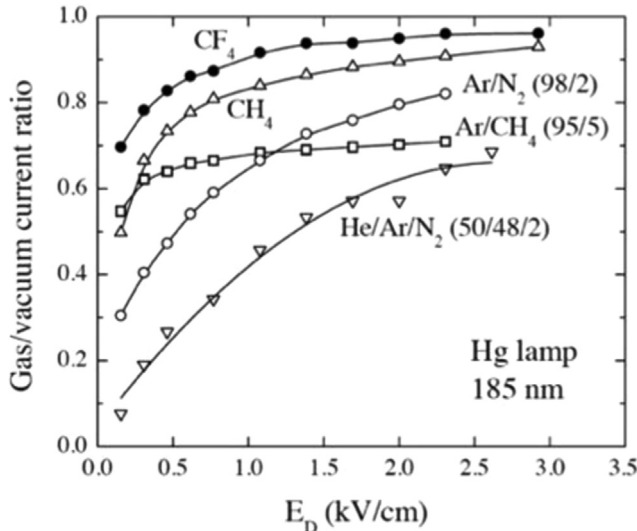


**Fig. 57.** Quantum efficiency relative to vacuum of CsI as a function of extraction field for several gases.

## 15. Dual-phase detectors

Even high pressure gases do not provide large enough cross-sections for detection of rare events in neutrino astrophysics and dark matter searches. Liquid noble gases are more appropriate, but they do not achieve the charge amplification needed to detect small ionization yields. A recently explored solution is to use dual-phase devices, where the primary interaction takes place in the liquid, and the ionization electrons are extracted by an external field into the overlying gas layer. Allowing at the same time the application of large extraction field near the liquid surface and charge multiplication, multi-GEM structures appear to be a very promising approach.

Fig. 71 shows the gain as a function of voltage for a Triple-GEM detector measured in the gas phase over liquid argon, krypton and xenon at cryogenic temperatures [141]; values of the electric field needed to extract electrons from the liquid into the gas are given

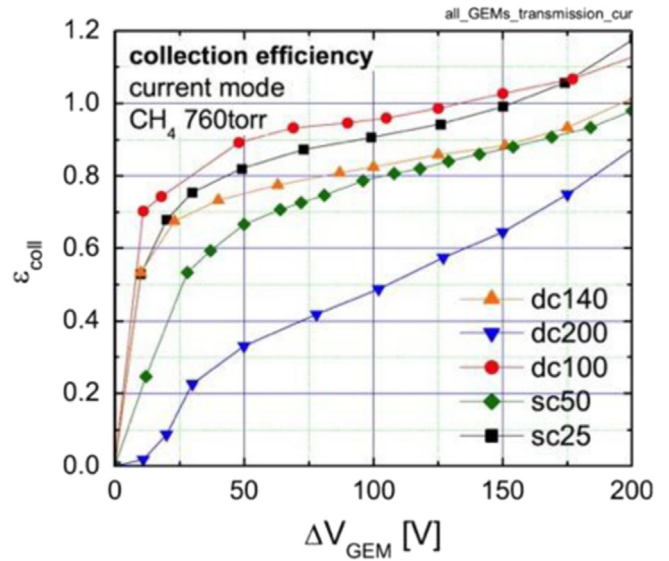


**Fig. 58.** Electron collection efficiency as a function of GEM voltage for several electrode designs.

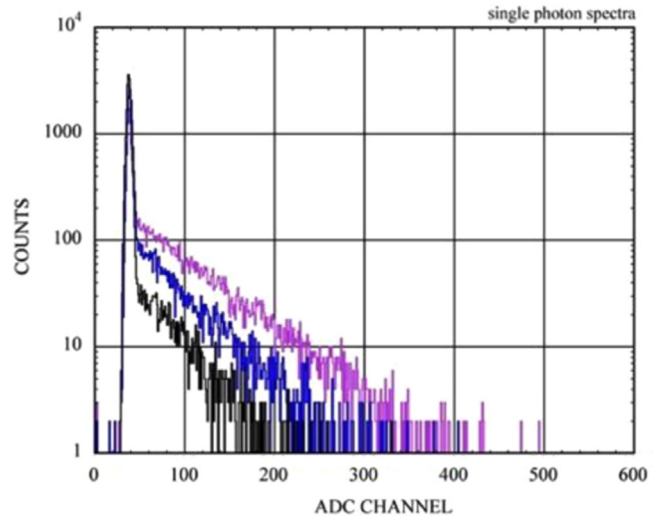


**Fig. 59.** Single photon pulse height spectra at increasing GEM gains.

in the inset. Gains are large enough to permit detection of single electrons [142]. Similar results have been obtained with Thick-GEM devices, more convenient of use in cryogenic conditions due to the use of self-supporting electrodes; a comparison of performances of standard and Thick-GEM detectors in liquid argon is given in Fig. 72 [143].

Large volume, dual phase TPC-like devices have been developed aiming at dark matter searches, using multi-GEM or large electron multipliers (LEM) as detectors in the gas phase. The time of the interaction, needed as reference for the reconstruction of the event, is provided by arrays of photomultipliers surrounding the sensitive volume, detecting the primary scintillation released in the interaction [51,144]. Alternatively, the UV photons emitted by scintillation can be detected with an internal CsI photosensitive layer deposited on the multiplying electrode itself [145].

Fig. 73 is an example of multi-track event recorded with a projective 2-D electronic readout system in the two-phase liquid argon LEM-TPC; the gray level of each segment is proportional to the signal amplitude [146].

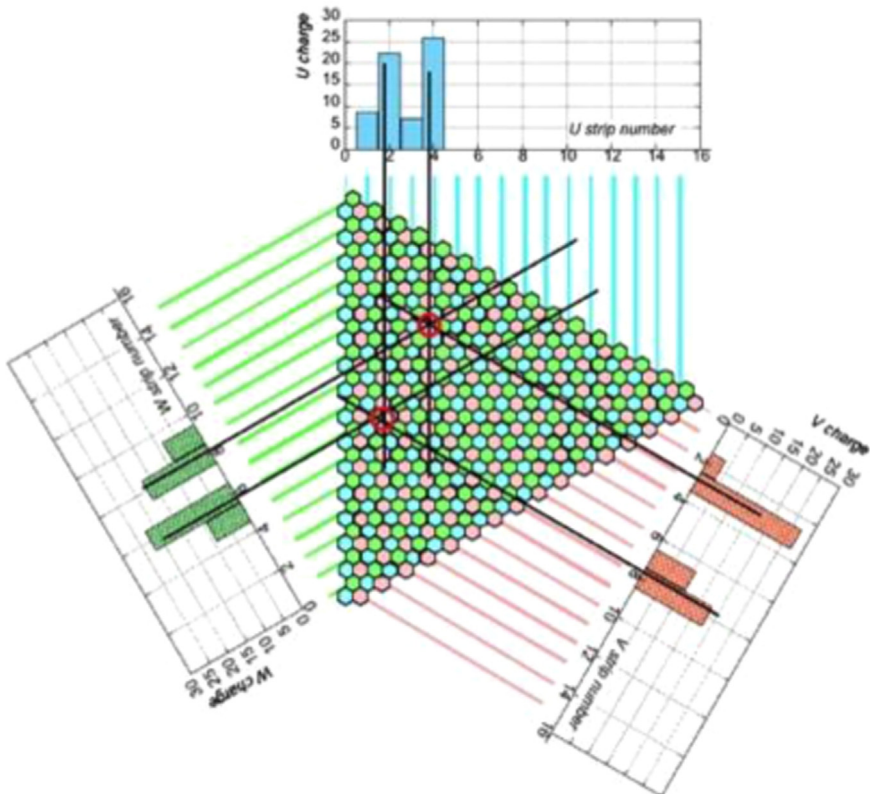


**Fig. 60.** A double-photon event recorded with the hexaboard readout. The projective strips pitch is 500  $\mu\text{m}$ .

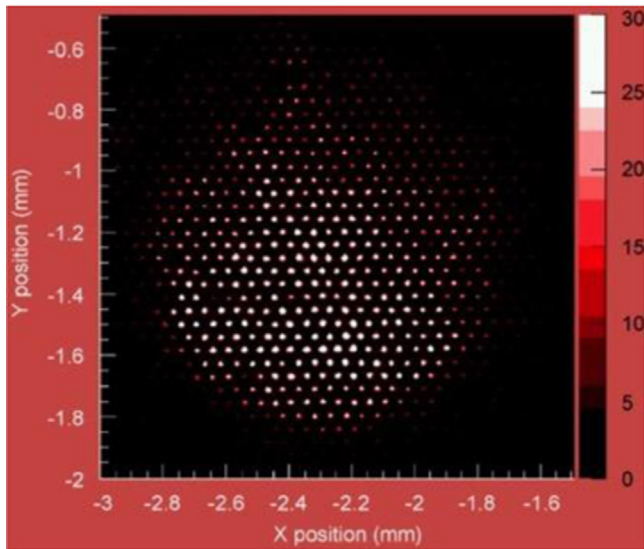


**Fig. 61.** Image of a micro-GEM foil illuminated by an UV source; the holes pitch is 50  $\mu\text{m}$ . A fit through the distributions provides an intrinsic hole localization accuracy of  $\sim 5 \mu\text{m}$  rms.

## 16. Optical GEM imagers

The inelastic collisions between electrons and molecules in high electric field result, aside from the charge multiplication exploited in most gaseous counters, in a copious emission of photons, with intensity and wavelength distributions characteristic of each gas. The secondary photon emission of GEM devices has been exploited for low-rate imaging of events with inexpensive solid state cameras as sensors, avoiding the need of sophisticated electronics recording systems. Two-dimensional localization

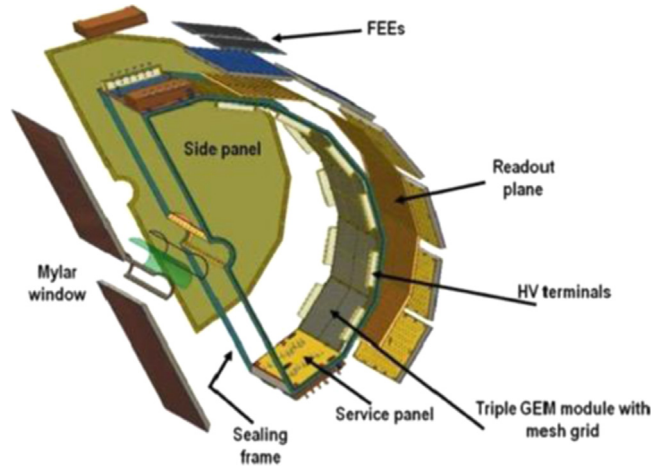


**Fig. 62.** Schematics of one sector of the HDB detector.

of soft X-ray events with 100  $\mu\text{m}$  accuracy was demonstrated using single-and double-GEM devices and a high resolution CCD camera [147]. While in most gases the emission is in the vacuum ultraviolet region, requiring the use of thin-layer wavelength shifters, mixtures of helium and carbon tetrafluoride have a copious emission around 600 nm, matching the spectral response of commercial cameras. Fig. 74 shows the optical image of overlapping neutron interactions in a GEM-based device with  ${}^3\text{He}-\text{CF}_4$  gas filling; the vertex of the interaction is clearly identified, and integration of the light yield over the track length provides the energy loss of the prongs [148].

The good proportionality between primary ionization losses and secondary light emission observed in GEM devices can be exploited to realize simple tools for dose determination in medical

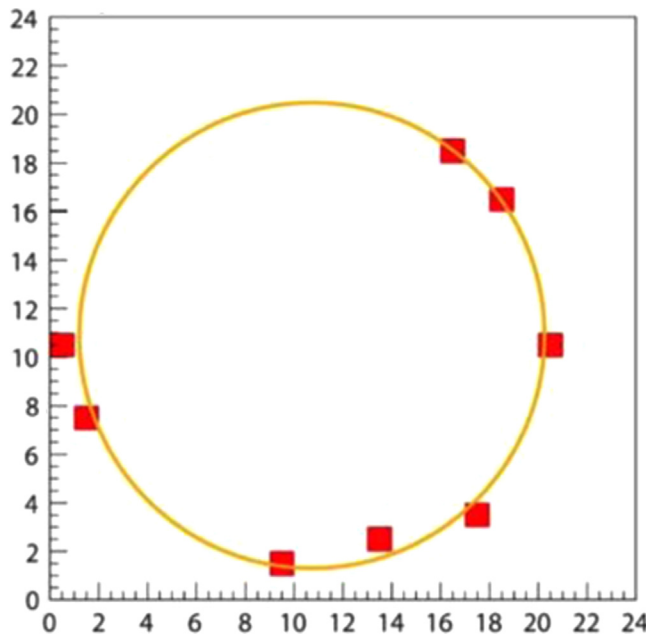


Fig. 63. An eight-photon ring detected with the COMPASS-RICH 1 prototype.

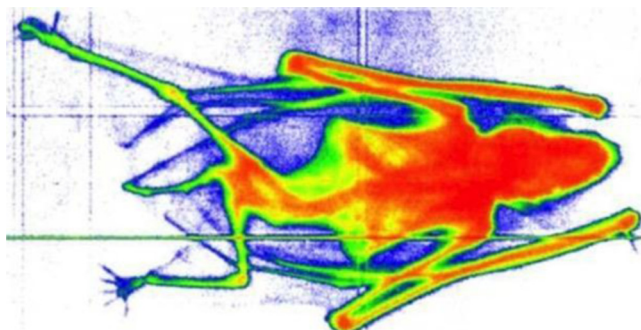


Fig. 64. Soft X-ray absorption radiography of a bat. The image size is about  $60 \times 20$  mm.

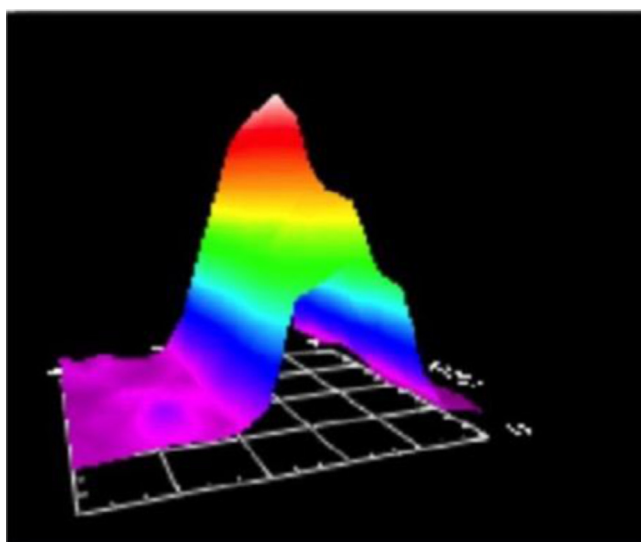


Fig. 65. Two-dimensional plasma soft X-ray activity.

diagnostics; due to the high intensity of the beams used for therapy, the GEM detectors can be operated at moderate gains with the solid state sensor placed at an angle with the detector to

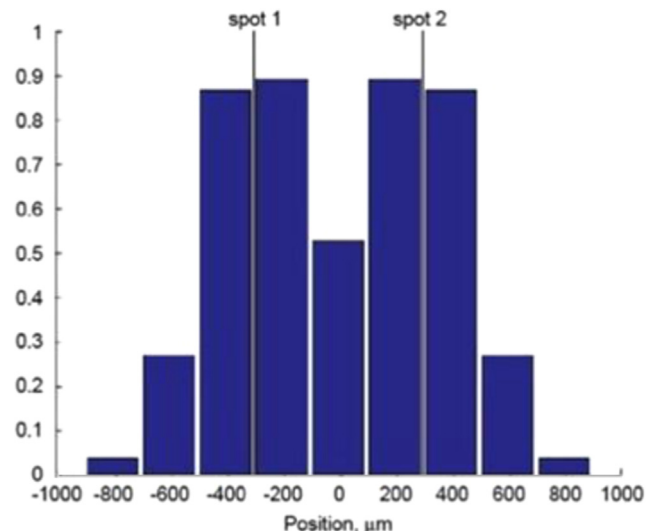


Fig. 66. Image of two X-ray diffraction spots  $0.1^\circ$  apart.

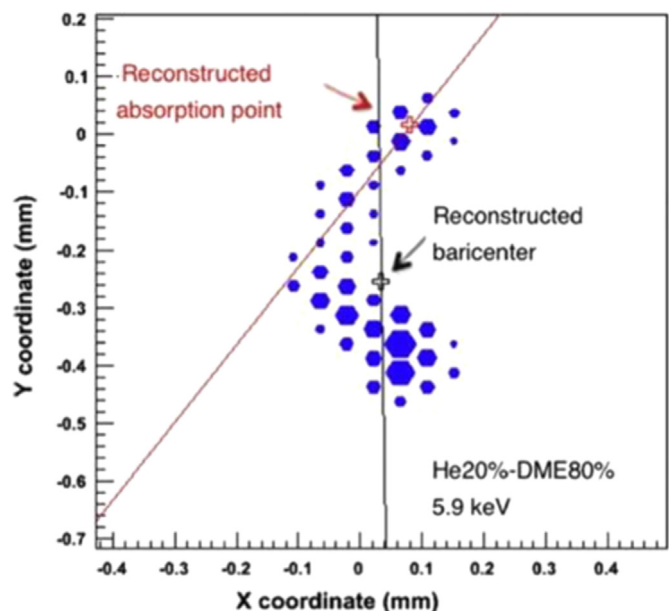


Fig. 67. A 5.9 photoelectron track recorded with the soft-X-ray polarimeter.

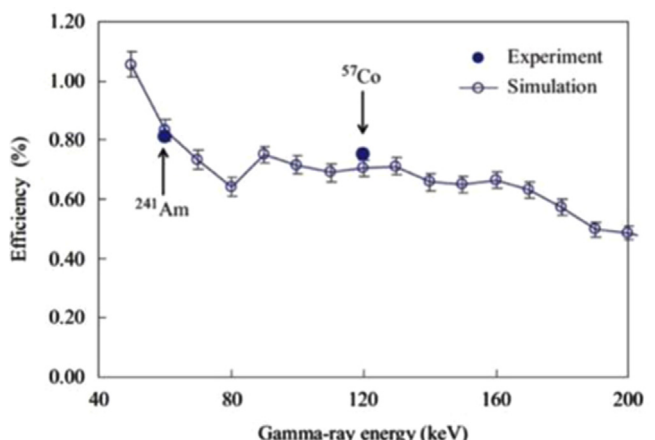
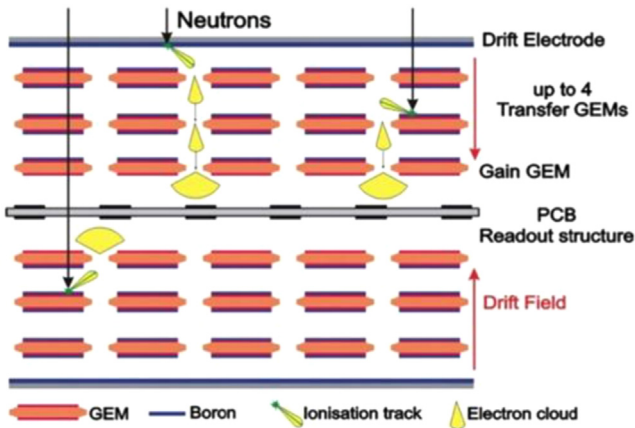
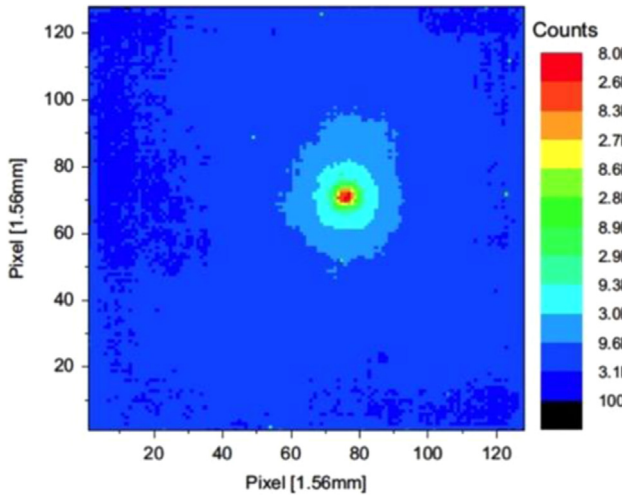


Fig. 68. Detection efficiency of a Au-plated GEM.



**Fig. 69.** Schematics of the CASCADE neutron detector.



**Fig. 70.** A two-dimensional image of a cold neutron beam, 0.57 mm in diameter.

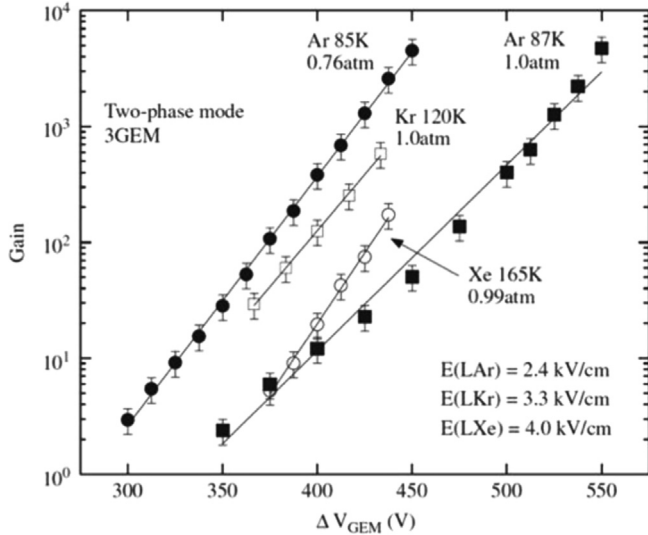


**Fig. 71.** Gain–voltage characteristics of a Triple-GEM in a dual-phase detector with liquid noble gas fillings. The corresponding values of the extraction field are given in the inset.

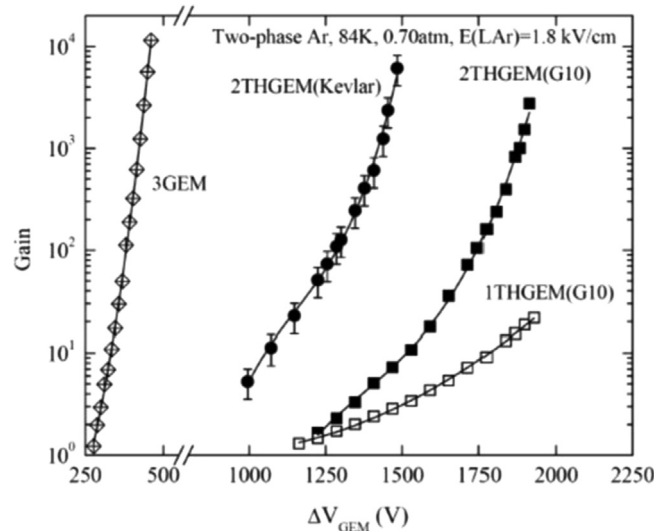


**Fig. 72.** Gain as a function of voltage in a dual-phase argon device with multiple thin and thick GEMs.

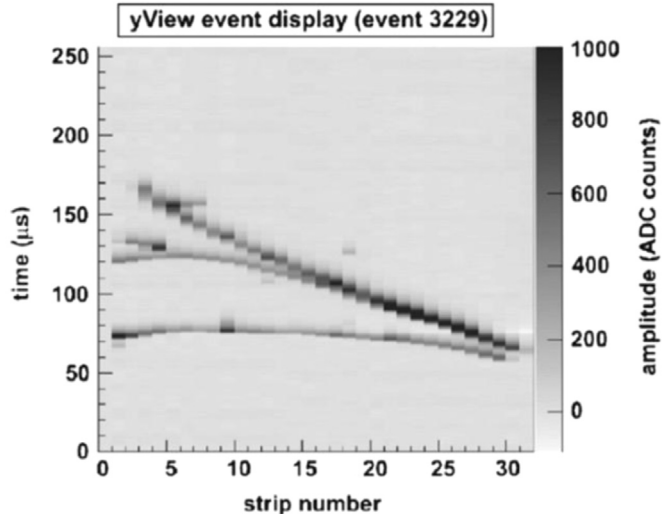


**Fig. 73.** A multi-track event recorded with a dual-phase argon TPC using a Large Electron Multiplier as charge sensor and photomultipliers to record the time of the interaction from primary scintillation in the liquid.



**Fig. 74.** Neutron conversions in  ${}^3\text{He}$  recorded with a solid state camera from the photon emission in a multi-GEM amplifier.

be outside the beam. For a 205 MeV beam, Fig. 75 is a comparison, as a function of the thickness of a water equivalent absorber in front of the detector, between the simulation results and signals recorded with a wide aperture ionization chamber, the charge and

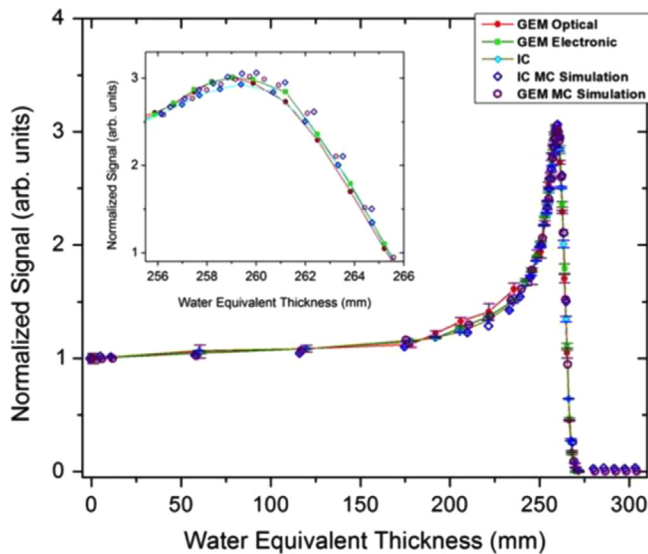


**Fig. 75.** Bragg peak recorded with various monitoring devices.

the light emission of a GEM detector. An expanded view in the region of the Bragg peak (inset) shows the excellent agreement between the various estimates [149].

## 17. Conclusions and outlook

The introduction in the late nineties of a variety of innovative devices, collectively named micro-pattern gaseous detectors, has substantially changed the world of gaseous radiation sensors. Thanks to the large development efforts of many groups, the understanding of the operating properties and the manufacturing technologies of the novel devices has progressed over the years, culminating with the construction and use in particle physics experiments of large arrays of performing detectors. For GEM devices, in particular, sensitive areas exceeding square meters, sub-mm position accuracy, single electron sensitivity, long-term operational stability and reliability have been demonstrated, suggesting their use as replacement of more conventional devices in detector upgrades motivated by the increased luminosity of the accelerators. Applications outside particle physics: astrophysics, medical diagnostics, biology have also been initiated, opening up new perspectives only briefly outlined in this review.

Concurrently with the development of the detectors, a big effort has been invested in the design and realization of custom integrated circuits matching the high granularity requirements of large setups. Originally developed for direct radiation detection, solid-state pixel circuits have been adapted to collect and record the charge released by ionization in the gas and amplified by a GEM- or Micromegas-like structure, integrated over the silicon sensor. Due to the large gas gain and the very low electrode capacitance, these devices have the potential to detect and image single ionization electrons, reaching the ultimate tracking precision of a gaseous counter [100,150].

## References

- [1] G. Charpak, et al., Nuclear Instruments and Methods 62 (1968) 262.
- [2] F. Sauli, *Gaseous Radiation Detectors*, Cambridge University Press, Cambridge, 2014.
- [3] A. Breskin, et al., Nuclear Instruments and Methods 124 (1974) 189.
- [4] M. Capeáns, Nuclear Instruments and Methods A 515 (2003) 73.
- [5] A. Oed, Nuclear Instruments and Methods A 263 (1988) 351.
- [6] F. Sauli, Nuclear Physics B – Proceedings Supplements 61 (1998) 236.
- [7] F. Sauli, A. Sharma, Annual Review of Nuclear and Particle Science 49 (1999) 341.
- [8] M. Titov, Nuclear Instruments and Methods A 581 (2007) 25.
- [9] S. Duarte Pinto, RD51, an R&D collaboration for Micropattern Gaseous Detectors, arXiv:0907.2673, 2009.
- [10] F. Sauli, Nuclear Instruments and Methods A 386 (1997) 531.
- [11] F. Sauli, Comprehensive Biomedical Physics 8 (2014) 367.
- [12] G. Charpak, F. Sauli, Physics Letters B 78 (1978) 523–528.
- [13] R. McCarty, et al., Nuclear Instruments and Methods A 248 (1986) 69.
- [14] S. Bachmann, et al., Nuclear Instruments and Methods A 438 (1999) 376.
- [15] W. Bonivento, et al., IEEE Transactions on Nuclear Science NS49 (2002) 1638.
- [16] V. Tikhonov, R. Veenhof, Nuclear Instruments and Methods A 478 (2002) 452.
- [17] P.S. Barbeau, et al., Nuclear Instruments and Methods A 525 (2004) 33.
- [18] A. Bressan, et al., Nuclear Instruments and Methods A 425 (1999) 254.
- [19] C. Büttner, et al., Nuclear Instruments and Methods A 409 (1998) 79.
- [20] A. Bressan, et al., Nuclear Instruments and Methods A 425 (1999) 262.
- [21] A. Bondar, et al., Nuclear Instruments and Methods A 496 (2003) 325.
- [22] K. Dehmelt, Performance of a Quintuple-GEM Based RICH Detector Prototype, arXiv:submit/1158752, 2015.
- [23] G. Corradi, et al., Nuclear Instruments and Methods A 572 (2007) 96.
- [24] A. Bressan, et al., Nuclear Instruments and Methods A 424 (1999) 321.
- [25] S. Bachmann, et al., Nuclear Instruments and Methods A 479 (2002) 294.
- [26] C. Altunbas, et al., Nuclear Instruments and Methods A 490 (2002) 177.
- [27] M. Alfonsi, et al., Nuclear Instruments and Methods A 518 (2004) 106.
- [28] A. Bressan, et al., Nuclear Instruments and Methods A 423 (1999) 119.
- [29] A. Buzulutskov, et al., Nuclear Instruments and Methods A 443 (2000) 164.
- [30] R. Chechik, et al., Nuclear Instruments and Methods A 419 (1998) 423.
- [31] A. Bondar, et al., Nuclear Instruments and Methods A 419 (1998) 418.
- [32] T.L. van Vuure, et al., IEEE Transactions on Nuclear Science NS48 (2001) 1092.
- [33] A. Bondar, et al., Nuclear Instruments and Methods 481 (2002) 200.
- [34] A. Bondar, et al., Nuclear Instruments and Methods 493 (2002) 8.
- [35] A. Orthen, et al., Nuclear Instruments and Methods A 512 (2003) 476.
- [36] T. Alexopoulos, et al., Nuclear Instruments and Methods A 640 (2011) 110.
- [37] J. Galán, et al., Nuclear Instruments and Methods 732 (2013) 229.
- [38] R. Oliveira, et al., Nuclear Instruments and Methods 576 (2007) 362.
- [39] V. Peskov, et al., Nuclear Instruments and Methods A 661 (2012) S153.
- [40] G. Bencivenni, et al., Journal of Instrumentation 10 (2014) P02008.
- [41] V. Peskov, et al., Journal of Instrumentation 7 (2012) C01005.
- [42] M. Ziegler, Development of a triple GEM detector for the LHCb experiment (Thesis at Universität Zürich), 2002.
- [43] M. Villa, et al., Nuclear Instruments and Methods A 628 (2011) 182.
- [44] M. Alfonsi, et al., Nuclear Instruments and Methods A 617 (2010) 151.
- [45] J. Benlloch, et al., Nuclear Instruments and Methods 419 (1998) 410.
- [46] B. Surrow, et al., Nuclear Instruments and Methods A 572 (2007) 201.
- [47] M. Inuzuka, et al., Nuclear Instruments and Methods A 525 (2004) 529.
- [48] T. Tamagawa, et al., Nuclear Instruments and Methods A 560 (2006) 418.
- [49] L. Periale, et al., Nuclear Instruments and Methods A 478 (2002) 377.
- [50] R. Chechik, et al., Nuclear Instruments and Methods A 535 (2004) 303.
- [51] A. Badertscher, et al., Nuclear Instruments and Methods A 617 (2010) 188.
- [52] M. Alexeev, et al., IEEE Nuclear Science Symposium Conference Record (2008) 1335.
- [53] T. Tamagawa, et al., Nuclear Instruments and Methods A 608 (2009) 390.
- [54] C. Shalem, et al., Nuclear Instruments and Methods A 558 (2006) 475.
- [55] P. Martinengo, et al., Nuclear Instruments and Methods A 639 (2011) 126.
- [56] H. Takahashi, et al., Nuclear Instruments and Methods A 724 (2013) 1.
- [57] Y. Xie, et al., Nuclear Instruments and Methods A 729 (2013) 809.
- [58] M. Alfonsi, et al., Nuclear Instruments and Methods A 671 (2012) 6.
- [59] U. Becker, et al., Nuclear Instruments and Methods A 556 (2006) 527.
- [60] F. Simon, et al., IEEE Transactions on Nuclear Science NS54 (2007) 2646.
- [61] G. Hamar, D. Varga, Nuclear Instruments and Methods A. 694 (2012) 16.
- [62] M. Kalliokoski, et al., Nuclear Instruments and Methods A 664 (2012) 223.
- [63] T. Hildén, et al., Nuclear Instruments and Methods A 770 (2015) 113.
- [64] P. Abbon, et al., Nuclear Instruments and Methods A 577 (2007) 455.
- [65] M.G. Bagliesi, et al., Nuclear Instruments and Methods A 617 (2010) 134.
- [66] M. Krämer, et al., IEEE Nuclear Science Symposium Conference Record (2008).
- [67] D. Abbaneo, et al., Nuclear Instruments and Methods A 732 (2013) 203.
- [68] S. Duarte Pinto, et al., IEEE Nuclear Science Symposium Conference Record (2008).
- [69] M. Tytgat, et al., Construction and performance of large-area triple-GEM prototypes for future upgrades of the CMS forward muon system, IEEE Nuclear Science Symposium N19 7 (2011) 1019.
- [70] D. Abbaneo, et al., Performance of a large-area GEM detector prototype for the upgrade of the CMS endcap system, IEEE NSS Conference Record (2014).
- [71] H. Fenker, et al., Nuclear Instruments and Methods A 592 (2008) 273.
- [72] A. Balla, et al., Nuclear Instruments and Methods A 732 (2013) 221.
- [73] M.J. French, et al., Nuclear Instruments and Methods A 466 (2001) 359.
- [74] B. Ketzer, et al., Nuclear Instruments and Methods A 535 (2004) 314.
- [75] S. Minutoli, et al., Nuclear Instruments and Methods A 718 (2013) 223.
- [76] A. Sharma, M. Tytgat, CMS Technical Design Report (2014).
- [77] M. Alfonsi, et al., IEEE Transactions on Nuclear Science NS52 (2005) 2872.
- [78] P. Everaerts, Rate capability and ion feedback in GEM detectors (Thesis at Gent University), 2006.
- [79] F. Murtas, et al., Nuclear Instruments and Methods A 617 (2010) 237.
- [80] D. Pacella, et al., Nuclear Instruments and Methods A 720 (2013) 53.
- [81] C. Altunbas, et al., Nuclear Instruments and Methods A 515 (2003) 249.

- [82] F. Sauli, GEM readout of the time projection chamber, CERN-EP-TA1 Internal Report (1999).
- [83] S. Kappler, et al., IEEE Transactions on Nuclear Science NS51 (2004) 1039.
- [84] S. Kappler, et al., IEEE Transactions on Nuclear Science NS51 (2004) 1524.
- [85] J. Kaminski, et al., GEM TPC Anode Pad Shape Studies, TPC Application Workshop, Berkeley CA (USA), 2006.
- [86] B. Ledermann, et al., Nuclear Instruments and Methods A 581 (2007) 232.
- [87] J. Kaminski, et al., Nuclear Instruments and Methods A 535 (2004) 201.
- [88] K. Dehmelt, Nuclear Instruments and Methods A 623 (2010) 97.
- [89] M.E. Janssen, et al., Nuclear Instruments and Methods A 566 (2006) 75.
- [90] S.X. Oda, et al., Nuclear Instruments and Methods A 566 (2006) 312.
- [91] H. Sako, et al., Nuclear Instruments and Methods A 763 (2014) 65.
- [92] M.S. Dixit, et al., Nuclear Instruments and Methods A 518 (2004) 721.
- [93] K. Boudjemline, et al., Nuclear Instruments and Methods A 574 (2007) 22.
- [94] L. Fabbietti, et al., Nuclear Instruments and Methods A 628 (2011) 204.
- [95] R. Arora, et al., Physics Procedia 37 (2012) 491.
- [96] B. Ketzer, Nuclear Instruments and Methods A 732 (2013) 237.
- [97] H. van der Graaf, et al., Nuclear Instruments and Methods A 566 (2006) 62.
- [98] H. van der Graaf, Nuclear Instruments and Methods A 580 (2007) 1023.
- [99] X. Llopart, et al., Nuclear Instruments and Methods A 581 (2007) 485.
- [100] V.M. Blanco Carballo, et al., Nuclear Instruments and Methods A 608 (2009) 86.
- [101] F. Sauli, et al., IEEE Transactions on Nuclear Science NS50 (2003) 803.
- [102] F. Sauli, et al., Nuclear Instruments and Methods A 560 (2006) 269.
- [103] W. Blum, G. Rolandi, Particle Detection with Drift Chambers, Springer-Verlag, Berlin, 1993.
- [104] M. Killenberg, et al., Nuclear Instruments and Methods A 530 (2004) 251.
- [105] ALICE\_Collaboration, Technical Design Report for the Alice Time Projection Chamber, 2014.
- [106] T. Gunji, Nuclear Physics A 931 (2014) 1152.
- [107] M. Ball, et al., Journal of Instrumentation 9 (2014) C04025.
- [108] P. Gasik, Journal of Instrumentation 9 (2014) C04035.
- [109] F.V. Böhmer, et al., Nuclear Instruments and Methods A 719 (2013) 101.
- [110] F.V. Böhmer, et al., Nuclear Instruments and Methods A 737 (2014) 214.
- [111] J. Va'vra, et al., Nuclear Instruments and Methods A 433 (1999) 527.
- [112] J. Va'vra, A. Sharma, Nuclear Instruments and Methods A 478 (2002) 235.
- [113] A. Breskin, et al., Nuclear Instruments and Methods A 483 (2002) 670.
- [114] M. Alexeev, et al., Nuclear Instruments and Methods A 617 (2010) 396.
- [115] T. Meinschad, et al., Nuclear Instruments and Methods A 535 (2004) 324.
- [116] D. Mörmann, et al., Nuclear Instruments and Methods A 504 (2003) 93.
- [117] D. Mörmann, et al., Nuclear Instruments and Methods A 530 (2004) 258.
- [118] F. Sauli, et al., IEEE Nuclear Science Symposium Conference Record (2004).
- [119] R. Bellazzini, et al., Nuclear Instruments and Methods 581 (2007) 246.
- [120] W. Anderson, et al., Nuclear Instruments and Methods A 646 (2011) 35.
- [121] M. Alexeev, et al., Journal of Instrumentation 7 (2012) C02014.
- [122] A. Alexeev, et al., Journal of Instrumentation 9 (2014) C09017.
- [123] V. Peskov, et al., Nuclear Instruments and Methods A 695 (2012) 154.
- [124] A. Breskin, et al., IEEE Transactions on Nuclear Science NS48 (2001) 417.
- [125] J.M. Maia, et al., Nuclear Instruments and Methods A 523 (2004) 334.
- [126] J.F.C.A. Veloso, et al., Nuclear Instruments and Methods A 639 (2011) 134.
- [127] J.A. Mir, et al., Nuclear Instruments and Methods A 580 (2007) 1372.
- [128] D. Pacella, et al., Review of Scientific Instruments 72 (2001) 1372.
- [129] J. Rzadkiewicz, et al., Nuclear Instruments and Methods A 720 (2013) 36.
- [130] E.A. Babichev, et al., Nuclear Instruments and Methods A 323 (1992) 49.
- [131] V.M. Aulchenko, et al., Nuclear Instruments and Methods A 603 (2009) 69.
- [132] R. Bellazzini, F. Muleri, Nuclear Instruments and Methods A 623 (2010) 766.
- [133] T. Koike, et al., Nuclear Instruments and Methods A 648 (2011) 180.
- [134] C. Iacobaeus, et al., IEEE Transactions on Nuclear Science NS48 (2000) 1496.
- [135] M. Wallmark, et al., Nuclear Instruments and Methods A 471 (2001) 151.
- [136] B. Gebauer, Nuclear Instruments and Methods A 535 (2004) 65.
- [137] M. Klein, C.J. Schmidt, Nuclear Instruments and Methods A 628 (2011) 9.
- [138] G. Croci, et al., Nuclear Instruments and Methods A 720 (2013) 144.
- [139] G. Croci, et al., Nuclear Instruments and Methods A 732 (2013) 217.
- [140] B. Esposito, et al., Nuclear Instruments and Methods A 741 (2014) 196.
- [141] A. Bondar, et al., Nuclear Instruments and Methods A 556 (2006) 273.
- [142] A. Bondar, et al., Nuclear Instruments and Methods A 574 (2007) 493.
- [143] A. Bondar, et al., Journal of Instrumentation 3 (2008) P07001.
- [144] P.K. Lightfoot, et al., Nuclear Instruments and Methods A 554 (2005) 266.
- [145] W. Xe, et al., Nuclear Instruments and Methods A 774 (2015) 120.
- [146] A. Badertscher, et al., Nuclear Instruments and Methods A 641 (2011) 48.
- [147] F.A.F. Fraga, et al., IEEE Nuclear Science Symposium Conference Record 2 (1999) 829.
- [148] F.A.F. Fraga, et al., Nuclear Instruments and Methods A 478 (2002) 357.
- [149] A.V. Klyachko, et al., Nuclear Instruments and Methods A 628 (2011) 434.
- [150] P. Colas, et al., Nuclear Instruments and Methods A 535 (2004) 508.